Process-based morphodynamic modeling of the Yangtze Estuary at a decadal timescale: Controls on estuarine evolution and future trends

Luan, Hualong; Ding, Ping Xing; Wang, Zhengbing ; Ge, Jian Zhong

DOI
10.1016/j.geomorph.2017.04.016

Publication date
2017

Document Version
Accepted author manuscript

Published in
Geomorphology

Citation (APA)
Luan, H., Ding, P. X., Wang, Z., & Ge, J. Z. (2017). Process-based morphodynamic modeling of the Yangtze Estuary at a decadal timescale: Controls on estuarine evolution and future trends. *Geomorphology*, *290*, 347-364. https://doi.org/10.1016/j.geomorph.2017.04.016

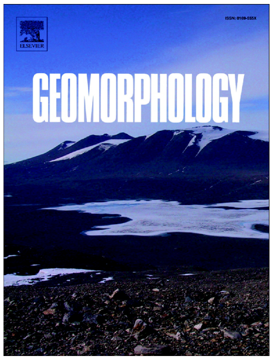

Process-based morphodynamic modeling of the Yangtze Estuary at a decadal timescale: Controls on estuarine evolution and future trends

Hua Long Luan, Ping Xing Ding, Zheng Bing Wang, Jian Zhong Ge

PII: S0169-555X(16)30935-7
DOI: doi: 10.1016/j.geomorph.2017.04.016
Reference: GEOMOR 5997

To appear in: *Geomorphology*

Received date: 27 September 2016
Revised date: 10 April 2017
Accepted date: 10 April 2017

Please cite this article as: Hua Long Luan, Ping Xing Ding, Zheng Bing Wang, Jian Zhong Ge , Process-based morphodynamic modeling of the Yangtze Estuary at a decadal timescale: Controls on estuarine evolution and future trends. The address for the corresponding author was captured as affiliation for all authors. Please check if appropriate. Geomor(2017), doi: 10.1016/j.geomorph.2017.04.016

Process-based morphodynamic modeling of the Yangtze Estuary at a decadal timescale: controls on estuarine evolution and future trends

Hua Long Luan [a, b], Ping Xing Ding [a, *], Zheng Bing Wang [a, b, c], Jian Zhong Ge [a]

[a] State Key Laboratory of Estuarine and Coastal Research, East China Normal University, Shanghai 200062, China

[b] Delft University of Technology, Faculty of Civil Engineering and Geosciences, 2628 CN Delft, The Netherlands

[c] Deltares, 2600 MH Delft, The Netherlands

*Corresponding author.

Tel: +86 021-62232897

Fax: +86 021-62233468

E-mail address: pxding@sklec.ecnu.edu.cn (Prof. P.X. Ding)

Highlights

- ✓ Promising hindcasting of the decadal morphodynamic evolution of the Yangtze Estuary
- ✓ Sediment grain size and variations in fluvial forcing are crucial for modeling
- ✓ Forecasting the estuarine morphodynamics to the year 2030 provides guidelines for management

Abstract

Understanding the decadal morphodynamic evolution of estuaries and deltas and their controls is of vital importance regarding management for estuarine function and sustainable development. This work addresses this issue by applying a process-based model system (Delft3D) to hindcast and then forecast the morphodynamic evolution of the Yangtze Estuary at a decadal timescale. Forced by the river and tides, the model considers sand-mud mixture and the variations of river water discharge and sediment discharge. The morphodynamic model is validated against three periods, i.e., an accretion period (1958-1978), an erosion period (1986-1997) and a recent accretion period with human activities (2002-2010). Model results show good performance with respect to spatial erosion and deposition patterns, sediment volume changes, and hypsometry curves. The model reveals quite different behaviors for mud transport between the dry and wet seasons, which is subject to the prescription of river boundary conditions and bed composition. We define six scenarios to project evolution to the year 2030 under decreased river inputs and increased relative sea level. The simulations reveal that overwhelming amount of erosion will likely occur in the inner and mouth bar area of the estuary. Particularly, the mouth zone will shift from net deposition before 2010 to net erosion by 2030, mainly because of decreasing sediment supply. Changes in water discharge have minor effects on the projected trend. Net erosion will be considerable when the sediment supply is extremely low (100 Mt yr^{-1}) due to the abundance of erodible modern sediment in the Yangtze Estuary. Erosion within the mouth bar area may be unexpected, including the deepening of the tidal inlet at East Chongming mudflat and the formation of a flood channel on the seaward side of Jiuduansha Shoal. Overall, the model results provide valuable information for sustainable delta management under changing conditions for both the Yangtze system and other similar estuaries and deltas with diminishing sediment supplies.

Keywords: Process-based modeling; Decadal morphological evolution; Variations of river inputs; Multiple sediment fractions; Yangtze Estuary

1. Introduction

Estuaries are semi-enclosed water bodies that are freely connected with terrestrial drainage and the open ocean, allowing the dilution of proximal saline ocean water by fresh river water (Cameron and Pritchard, 1963). With their high economic and ecological value, estuaries and deltas associated with mega-cities around the world have attracted attention in terms of environmental and geomorphological issues (Woodroffe et al., 2006; Syvitski and Saito, 2007). Under climate change and intensive human activities in recent decades, estuaries and deltas are faced with a series of growing threats including coastal flooding, infrastructure failure, reduction in the amounts of freshwater resource, and wetland ecosystem deterioration (Syvitski, 2008). A quantitative assessment of the changing risk profiles of major deltas around the world conducted by Tessler et al. (2015) indicates that current short-term strategies (years to decades) for risk reduction will likely increase relative risks without creating a sustainable long-term solution (decades to centuries). Scientists have called on both national and international governments to expand monitoring and forecasting research to protect inhabited deltas (Giosan et al., 2014). Therefore, the morphodynamic evolution of these dynamic systems in the coming decades to century must be investigated to provide a scientific basis for strategies and measures in response to future global changes.

The erosion and deposition patterns in estuaries and deltas largely depend on the fluvial sediment supply. Due to river damming and land-use changes, the sediment loads of many rivers have decreased dramatically (Walling and Fang, 2003), which has triggered delta erosion and drowning under superimposed impact of global sea-level rise (Milliman, 1997; Syvitski et al., 2009). Understanding and predicting estuarine morphodynamics is challenging because of the high uncertainty of upstream human activities and local engineering projects. The nonlinear interactions between hydrodynamics (e.g., tides, wind-driven waves, and river flow) and sediment transport (e.g., sand, mud, and mixtures of the two) determine the morphological development of an estuary at various temporal and spatial scales (Galloway, 1975; Dalrymple et al., 1992; Orton and Reading, 1993). Numerous case studies on estuarine and deltaic morphodynamics based on topographic and bathymetric dataset have been published in the past several decades (e.g., Gagliano et al., 1981; Stanley, 1996; Day et al., 2000; Van der Wal et al., 2002; Blott et al., 2006; Jaffe et al., 2007; Garel et al., 2014; Anthony et al., 2015). Although these data-driven studies have greatly improved our understanding of the processes and causes of the morphological development of estuaries and deltas, they cannot be used to generate predictions of morphological development due to the intrinsic feedback between physical processes and morphological behaviors. In other cases, high-resolution and successive bathymetric data are rare or unavailable; thus the demand for modeling methods is high.

The number of developed morphodynamic modeling techniques has been increasing (Roelvink, 2006) and these techniques have been incorporated into process-based model systems, e.g., Delft3D (Lesser et al., 2004), ROMS (Warner et al., 2008), Telemac (McCann，2011), and FINEL2D (Dam et al., 2016). For medium- to long-term morphodynamic modeling, one robust technique for bridging the scale gap between hydrodynamics and morphodynamics is accelerated bed-level updating, i.e., the morphology accelerating factor (MF). When using this technique, the bed-level change calculated for each hydrodynamic time step is multiplied by a user-defined MF to represent the bathymetric changes during an up-scaled period. Thus, the feedback mechanism between flow and morphology is well coupled. A sensitivity analysis by Roelvink (2006) indicated that the distortion induced by MF is acceptable if the bed-level variation within one tidal cycle is small relative to the local water depth (<10%). Equipped with the MF approach, the process-based model system Delft3D, for instance, has been widely employed in schematized modeling and has produced remarkable results (Hibma et al., 2003; Van der Wegen and Roelvink, 2008; Guo et al., 2014). Particular attention has been paid to long-term morphodynamic equilibrium of alluvial estuaries under tidal influences. Canestrelli et al. (2014a) schematized the Lower Fly River (Papua New Guinea) in a 1D morphodynamic model and a dynamic equilibrium was attained under a small sediment discharge. Bolla Pittaluga et al. (2015) numerically demonstrated the existence of equilibrium bed profile of tide-dominated alluvial estuaries without landward tidal wave amplification. Inspired by the Yangtze Estuary, Guo et al. (2014, 2015a) also identified the effects of river discharge and its seasonality on the morphodynamic equilibrium. Zhou et al. (2017) argued that modeling studies on morphodynamic equilibrium over appropriate spatial-temporal scales facilitate understanding the dominant processes in specific systems. Similarly, Ganju et al. (2009, 2011) applied the ROMS model with the MF method to simulate decadal morphological changes in Suisun Bay, California, and forecasted the morphological evolution of the bay for 2010-2030 considering future climate change and sediment supply scenarios (Ganju and Schoellhamer, 2010). To consider the inter-annual variations of the river discharge hydrograph, composite model results are obtained based on separated simulations forced by three typical hydrographs with varying occurrence possibilities. Van der Wegen and Roelvink (2012) successfully reproduced the bathymetry of the Western Scheldt estuary from an initially flat bathymetry using Delft3D. Dam et al. (2016) hindcasted the centennial morphological evolution of the Western Scheldt estuary using an unstructured 2D process-based model (FINEL2D), which showed that the accuracy of the model improved over the modeling time. These authors attributed their results to the morphological evolution constraints, including the estuarine geometry and erosion-resistant bed. Dissanayake et al. (2012) modeled the morphological response of a small tidal basin to human interference and achieved better results when multiple sediment fractions (mud and sand) were included rather than a single fraction. Van der Wegen et al. (2011a) also significantly improved the performance of their model of San Pablo Bay by considering multiple sediment fractions. Moreover, a 30-year forecast simulation suggested that accretion along the channel-flat interface may decrease or net erosion may occur as the fluvial sediment supply decreases (Van der Wegen and Jaffe, 2014). Van der Wegen et al. (2011a) schematized a hydrograph into 1 month of high discharge and 4 months of low discharge with different MFs to account for high variations of river inputs. Wang et al. (2014) forecasted the centennial morphological response of Tieshan Bay in Southwest China to dredging using FVCOM. Wei and Wu (2014) simulated the Holocene development of the Pearl River Delta and produced results that agreed well with sedimentation and stratigraphic data. The above review demonstrates the capabilities of process-based morphodynamic models for hindcasting the medium- to long-term morphological evolution of estuaries and deltas.

This work focuses on the morphodynamic evolution of the Yangtze Estuary at a decadal timescale by means of a process-based model. This large-scale estuary and its delta represent one of the most populous and prosperous regions in China, indicating its social-economic and environmental significances (Fig. 1b). River sediment discharge has significantly decreased since the 1980s due to the construction of dams in the upstream watershed, which has subsequently resulted in erosion of the subaqueous delta (Yang et al., 2011) and decreased the accretion rate of the intertidal flats (Yang et al., 2005). Numerous short-term (hours to days) field measurements of flow, salinity and sediment transport have been conducted and multiple relevant processes are identified, mostly characterized by strong vertical variations, such as estuarine gravitational circulation (Liu et al., 2011), salt and/or sediment-induced stratification (Song et al., 2013), sediment trapping and resuspension (Li and Zhang, 1998; Wu et al., 2012) and near-bed fluid mud (Wan et al., 2014). The combined effects of these processes influence the sedimentation processes in the Yangtze Estuary, particularly in the turbidity maximum. These works also demonstrate the complexity of fine sediment behavior and morphological evolution within this large-scale estuary. The morphodynamics of the Yangtze Estuary has been extensively studied in past decades. Most previous studies addressing morphological evolution processes are based on historical bathymetric data (Chen et al., 1985, 1999; Yang et al., 2003a, 2005, 2011; Wang et al., 2013; Dai et al., 2013, 2014, 2016; Li et al., 2016; Wei et al., 2016; Ding et al., 2016), whereas the controlling mechanisms and the future evolution trends have rarely been discussed using a process-based modeling approach. Hu et al. (2009) projected the evolution of Jiuduansha Shoal for 20 years assuming a decreasing sediment supply by using a well-calibrated Delft3D model; however the nearly linear evolution that was obtained was somewhat oversimplified because the interpretation was isolated to the estuary. Guo et al. (2013) simulated the 50-year evolution of the South Branch and reasonably approximated the channel-shoal pattern. Both studies only modeled parts of the Yangtze Estuary, and their models considered annual mean water and sediment discharge without strong seasonal river inputs, which is thought to affect the morphodynamics of the estuary. For example, high river discharge is thought to play an important role in accelerating morphological changes in the Yangtze Estuary (Yun, 2004; Luan et al., 2016). Therefore, high variations of river inputs, especially high discharge conditions, are important for morphological modeling of this large-scale estuary. Kuang et al. (2013) applied monthly-averaged river inputs and forecasted the evolution of tidal flats at the delta front after the closure of the Three Gorges Dam, but did not discuss the importance of high river flow. Additionally, Hu et al. (2009) suggested that multiple sediment fractions, including mud, are necessary to model sediment transport well in the Yangtze Estuary. However, the importance of the sand and mud mixture for morphodynamic evolution remains unknown, given that there are strong spatial variations of the bed sediment composition (Liu et al., 2010).

In the companion paper of this study (Luan et al., 2016), we analyzed the decadal morphological changes throughout the Yangtze Estuary between 1958 and 2010 and demonstrated that fluvial sediment reduction, river flooding, and estuarine engineering projects were the main driving forces of the decadal changes. To further validate our statement, we apply a process-based Delft3D model system in this study to hindcast and forecast the decadal morphological changes of the entire Yangtze Estuary. The variations of river flow and sediment discharge and the variations of multiple sediment fractions are included in the model. The morphological model is validated by hindcasting three periods with distinct evolutionary features, i.e., an accretion stage (1958-1978), an erosion stage (1986-1997) and a recent accretion stage with human activities (2002-2010), as described by

Luan et al. (2016). The validated morphological model can predict morphological changes through to the year 2050 or even 2100, but the reliability of the prediction decreases as the simulated period is extended. In this study, we conduct 20-year forecast modeling (2010-2030) based on six scenarios with decreasing river inputs and relative sea-level rise (RSLR). The simulations show erosion/deposition patterns and sediment volume changes and provide scientific data for guiding the sustainable management of the Yangtze Estuary.

2. The Yangtze Estuary and its river inputs

The Yangtze Estuary is a large-scale bifurcated channel system located on the west coast of the East China Sea (Fig. 1a). Luan et al. (2016) provide a detailed description of the estuary and the estuarine engineering projects. Thus we provide only a brief introduction of the estuary system. Fresh water and fine sediment from the catchment are delivered to the river mouth and exhibit strong seasonal variations. The mean monthly discharge during the wet and dry seasons ranges from 40,000-60,000 $m^3 s^{-1}$ and 10,000-20,000 $m^3 s^{-1}$, respectively, and the recorded daily discharge ranges from 4,260 $m^3 s^{-1}$ to 92,600 $m^3 s^{-1}$ (Shen et al., 1986). These ranges suggest the possible occurrence of extreme flood and drought events. Furthermore, the tide varies by a mean range of 2.6 m, which allows large amounts of water to enter the estuary through bifurcated channels and forms a tidal prism that is nearly ten times greater than the river discharge. The tidal signal can extend 600 km upstream to Datong (the tidal wave limit) during the dry season. Therefore, the Yangtze Estuary is classified as a long tidal basin and is influenced by significant river forcing (Guo et al., 2015b).

More than 99% of the sediment passing through Datong is suspended load and consists of silt and clay (Yang et al., 2003a), with an annual median grain size of ~10 μm (CWRC, 2011). In the Yangtze Estuary, the bed composition is highly graded with an apparent seaward-fining trend. Specifically, the bed consists of non-cohesive fine sand in the inner estuary and cohesive clayey silt and clay in the mouth bar area (Liu et al., 2010). The inner estuary and mouth bar area used in this study are defined in Luan et al. (2016) as mentioned in Section 3.7. Laterally, fine sand is often found in deep channels along the South Branch, and the main channels in the mouth bar area are mainly covered by silt and clay. This spatial distribution of the bed composition is thought to affect the morphological evolution of the Yangtze Estuary.

3. Model setup

3.1 Applied model

This study applies the process-based and fully integrated numerical model system Delft3D, which solves the shallow water equations under the hydrostatic pressure assumption. Delft3D uses a horizontal curvilinear grid with sigma layers for vertical variation. The model considers the major physical processes of coastal and estuarine systems, including the astronomic tide, fresh water discharge, salinity mixing, wind waves (offline and online), sediment transport (cohesive, non-cohesive and interactions), and online bed-level updating based on mass conservation (see more details in Lesser et al., 2004). Previous studies have demonstrated that Delft3D with proper model parameter settings can reproduce the detailed hydrodynamic patterns, complex sediment transport processes and historical morphological changes of the large-scale Yangtze Estuary at various timescales (Hu et al., 2009; Pan et al., 2012; Ying et al., 2012; Kuang et al., 2013). The model is used in 2DH mode in this study, which means that only depth-averaged processes are simulated. Secondary flow is included making the model quasi-3D.

3.2 Model domain

The model domain (Fig. 2) encompasses the entire Yangtze Estuary (upstream to Datong), Hangzhou Bay and the adjacent East China Sea. The spatial ranges of the domain in the west-east and north-south directions are 580 km and 450 km, respectively. The cell size varies from ~300 m within the estuary to ~3000 m near the offshore boundary. The model grid (Fig. 2) is a compromise between sufficient resolution and the greatest computational efficiency. Because the estuary is characterized by large-scale channel-shoal systems with spatial scales on the order of 10 km, the grid resolution of the present model is sufficient for simulating morphological behavior with acceptable accuracy. The offshore boundary is located near the 50 m isobath in the East China Sea and is ~125 km east of the 10 m isobath in the mouth bar area. The domain is large enough to eliminate the effects of possible boundary condition errors in the area of interest. The time step of the hydrodynamic model according to the CFL criteria is 2 min (Courant number <10). The impacts of the jetties and groins along the North Passage are represented by Current Deflection Wall (CDW).

3.3 Offshore boundary conditions

The offshore boundaries were driven by 8 main astronomic components (M2, S2, K1, O1, N2, K2, P1, and Q1) derived from a well-validated large model covering the East China Sea (Ge et al., 2013). Neap-spring variations are strong in the area. Our model began and ended bed-level updating during the neap tide to minimize errors caused by not using a full cyclic period. Calibrations of the model against tidal harmonics, water level and flow velocity indicate that the model effectively reproduces the tidal system and flow patterns around the Yangtze Estuary (refer to the Supplementary material, online). Monthly averaged salinity data digitized from the Editorial Board for Marine Atlas (1992) was prescribed along the offshore boundaries, which is only used for a simple flocculation model. The sediment concentrations at the offshore boundaries, which are far away from our study area, are set to zero. The Thatcher-Harleman time lag of 120 min is applied to the open boundaries, which means that the sediment returns when the tide returns (Deltares, 2014).

3.4 River boundary conditions

At the river boundary, time-series of water discharge (WD) and suspended sediment concentration (SSC) are prescribed at Datong, which is the seaward-most gauging station free of tidal influence. The WD and suspended sediment discharge (SSD) at Datong show strong seasonal variations (Fig. 3) with more concentrated SSD than WD during the wet season. Specifically, high WD occurs in July, and high SSD occurs in July, August and September (Fig. 3). Low WD and SSD occur during the dry season (December, January and February), and low SSD lasts until March. The remaining calendar months are characterized by intermediate WD and SSD. Schematization of river boundary conditions is required due to high computation effort when involving in morphological modeling at a decadal timescale. To account for the variations of WD and SSD without losing relevance, we schematized the annual river inputs into six periods (P1-P6, see Table 1) for each morphological hindcast case with different combinations of WD and SSD within 1 calendar year (Table 1). Monthly averaged values are applied for P2 (March) and P4 (July), and multiple monthly averaged values are applied for the remaining periods. One advantage of the river inputs schematization is that the yearly total amounts of water and sediment match the observed values, although the peak flood discharge (>60,000 $m^3 s^{-1}$) is flattened. After two months spinning up in the model, the bed-levels were allowed to change in the P1 when low river discharge conditions are applied. The six periods (P1-P6) are run sequentially in the morphological simulations as shown in the Table 1. The WD and SSD are constant during each period, typically representing 1-2 morphological years in combination with the MF approach (see Section 4.1). In other words, the variations in river discharges are taken into account instead of their seasonality. Guo et al. (2015a) compressed a yearly hydrograph to include seasonal river discharge in the model, which led to a decreased timescale of seasonal variations. This may cause unrealistic interactions between seasonal river flows and neap-spring tidal cycles due to their close timescales especially in this study. Nevertheless, the present schematization method was demonstrated to be capable for hindcasting decadal estuarine evolution (van der Wegen et al., 2011a), and also produces reasonable results for morphological hindcast of the Yangtze Estuary (see Section 4.3 for detailed description). Since the model domain includes Hangzhou Bay and the Qiantang River, a constant WD of 1,000 $m^3 s^{-1}$ is prescribed. The mean annual sediment discharge of Qiantang Estuary is 6.59 Mt/yr, which is negligible compared with the amount of the Yangtze Estuary. Moreover, Qiantang-derived sediment seldom reaches the Yangtze Estuary, since that the residual current and sediment transport in both summer and winter seasons are southward, i.e., from the Yangtze Estuary to the Hangzhou Bay (Hu et al., 2000). Therefore, no sediment supply is prescribed at the Qiantang Estuary.

3.5 Wind and waves

Wave parameters are calculated using the SWAN model (http://www.swan.tudelft.nl), which is driven by monthly climatological wind data (1995-2005) obtained from NCDC/NOAA Blended Sea Winds (http://www.ncdc.noaa.gov/oa/rsad/air-sea/seawinds.html). The wave information obtained each hour is coupled with the hydrodynamic and morphological model offline. Although storm episodes can induce significant changes over short periods (days) in shallow intertidal zones, extreme weather conditions, such as storm events and cold fronts, are beyond the scope of this study and are not considered in our model (Yang et al., 2003b).

3.6 Sediment transport model

The sediment transport processes responsible for bed-level changes vary greatly within the Yangtze Estuary due to the spatial variations of the bed sediment grain size, as mentioned in Section 2. Therefore, our model considers both non-cohesive (sand) and cohesive sediment (mud), which are treated separately in Delft3D, and sand-mud interactions are excluded as a first approximation. Suspended sediment transport is calculated by solving the depth-averaged advection-diffusion equation, which includes source and sink terms and is presented below:

$$\frac{\partial hc_i}{\partial t}+\frac{\partial huc_i}{\partial x}+\frac{\partial hvc_i}{\partial y}=\frac{\partial}{\partial x}\left(h\varepsilon_h\frac{\partial c_i}{\partial x}\right)+\frac{\partial}{\partial y}\left(h\varepsilon_h\frac{\partial c_i}{\partial y}\right)+S_i \qquad (1)$$

where h is the water depth (m), c_i is the sediment concentration of the i th sediment fraction (kg m^{-3}), u and v are horizontal velocity components (m s^{-1}), ε_h is the horizontal eddy diffusivity (m^2 s^{-1}), and S_i is the source and sink term of the i th sediment fraction representing the exchange between the water column and the bed.

For non-cohesive sediment transport ($\geq$ 64 μm), we follow the approach of Van Rijn

(1993), who defines sediment transport above and below the reference height a as the suspended load and bed load, respectively. The reference height is estimated as follows:

$$a = \min\left[\max\left\{Fac \cdot k_s, \frac{\Delta r}{2}, 0.01h\right\}, 0.20h\right] \tag{2}$$

where Fac is a user-defined proportionality factor, k_s is the user-defined effective roughness height related to current, and Δr is the wave-induced ripple height (0.025 m). The reference sediment concentration proportional to the relative sediment availability in the top layer of the bed is imposed at the reference height to entrain sediment to the water column. The medium grain diameter of the sand fraction is a dominant parameter that is used to determine the settling velocity according to Van Rijn (1993) and the critical depth-averaged velocity for the initiation of non-cohesive sediment based on the Shields curve. The settling velocity of the sand fraction is described as follows:

$$w_{s,i} = \begin{cases} \dfrac{(s_i - 1)gD_{50,i}}{18\nu} & 65\mu m < D_{50} < 100\mu m \\ \dfrac{10\nu}{D_{50,i}}\left(\sqrt{1 + \dfrac{0.01(s_i - 1)gD_{50,i}^3}{\nu^2}} - 1\right), & 100\mu m < D_{50} \le 1000\mu m \\ 1.1\sqrt{(s_i - 1)gD_{50,i}} & 1000\mu m < D_{50} \end{cases} \tag{3}$$

where s_i is the relative density ρ_s / ρ_w of the i th sand fraction, $D_{50,i}$ is the representative diameter of the i th sand fraction (m), and ν is the kinematic viscosity coefficient of water (m^2 s^{-1}). The bed-load transport under combined flow and waves is calculated using the following method developed by Van Rijn (1993):

$$\left|S_b\right| = 0.006\rho_s \omega_s D_{50} \frac{u_{eff}\left(u_{eff} - u_{cr}\right)^{1.4}}{\left[\left(s - 1\right)gD_{50}\right]^{1.2}} \tag{4}$$

where $\left|S_b\right|$ is the bed-load transport (kg m^{-1} s^{-1}), u_{eff} is the combined velocity magnitude of the depth-averaged flow velocity and near-bottom peak orbital velocity based on the significant wave height (m s^{-1}), and u_{cr} is the critical depth-averaged velocity for initiation of non-cohesive sediment based on the Shields curve (m s^{-1}). The effect of bed slope on bed-load transport is calculated according to Bagnold (1966) and Ikeda (1982).

The erosion and deposition fluxes of cohesive sediment (<64 μm) are calculated applying the following Partheniades-Krone formulations (Partheniades, 1965):

$$E_i = M_i\left(\frac{\tau_{cw}}{\tau_{ce,i}} - 1\right),\ \text{when}\ \ \tau_{cw} > \tau_{ce,i}\,,\ \text{else}\ \ E_i = 0 \tag{5}$$

$$D_i = w_{s,i} c_{b,i} \tag{6}$$

where E_i, D_i and M_i are the erosion flux, deposition flux and erosion parameter of the i th mud fraction (kg m^{-2} s^{-1}), respectively; $w_{s,i}$ is the settling velocity of the i th mud fraction (m s^{-1}); $c_{b,i}$ is the depth-averaged concentration of the i th mud fraction (kg m^{-3}); τ_{cw} is the combined bed shear stress due to currents and waves (N m^{-1}); and $\tau_{ce,i}$ is the critical shear stress for erosion of the i th mud fraction (N m^{-2}). The critical shear stress for deposition is omitted in the model following the suggestion of Winterwerp (2007), which means that continuous deposition is specified in the model.

3.7 Sediment parameters and initial bed compositions

Samples of the bed sediment of the Yangtze Estuary were collected in September 2015 and analyzed in terms of grain size and composition (Fig. 4). The results indicate that the bed composition within the Yangtze Estuary is highly variable in space. The inner estuary and mouth bar area are mainly covered by fine sand and clayey silt, respectively (Fig. 5), which is consistent with the results described by Liu et al. (2010). The median grain size (D_{50}) varies widely from ~5 to ~250 μm (Fig. 4). Therefore, multiple sediment fractions are considered in the morphological model. Specifically, two sand fractions are included in the model, i.e., the dominant fine sand fraction (s1, 100 μm) and a coarser sand fraction (s2, 300 μm), to reduce the overestimation of erosion along the channels. Additionally, four mud fractions (fine to coarse: m1~m4) are included to represent nearly the full range of cohesive sediment grain sizes (4, 7.5, 30, and 62.5 μm; Table 2). The settling velocity of each mud fraction (Table 2) is determined relative to the grain size after calibrating the model against the spatial distribution of the depth-averaged SSC. A simplified flocculation model that relates the floc settling velocity to the water salinity is applied (Deltares, 2014). The floc settling velocity is maximum (5 mm s^{-1}) when the salinity is greater than 8 psu (Hu et al., 2009).

The critical erosion shear stresses in the inner estuary and mouth bar area are defined separately to account for the strong variability of the bed composition. In the inner estuary, the following formulas are used (WUHEE, 1960; Du et al., 2010):

$$u_e = \left(\frac{h}{D_{50}} \right)^{0.14} \left(\alpha_1 \frac{\rho_s - \rho}{\rho} + \alpha_2 \frac{10 + h}{D_{50}{}^{0.72}} \right)^{0.5} \tag{7}$$

$$\tau_{ce} = K_e \rho \left[u_e / \left(2.5 \ln \left(11h / \Delta \right) \right) \right]^2 \tag{8}$$

where u_e and τ_{ce} are the critical erosion velocity and shear stress, respectively; ρ_s is the specific sediment density, 2650 kg m^{-3}; ρ is the fresh water density, 1000 kg m^{-1}; α_1 and α_2 are constant parameters, 17.6 and 6.05×10^{-7}, respectively; Δ is the roughness height, 1 mm; and K_e is a spatially varying coefficient that depends on the local sediment properties and ranges from 0.1 to 0.85 after model calibrations. For the mouth bar area where deposition and resuspension are frequent, the following soil mechanics-based method (Smerdon and Beasley, 1959; Torfs, 1995; Jacobs et al., 2011) is used to estimate τ_{ce}:

$$\tau_{ce} = \gamma_{cr} PI^{\beta} \tag{9}$$

where PI (%) is the plasticity index. The parameters γ_{cr} =0.161 and β =0.45 are used in our model. The PI varies linearly with the clay content (Skempton, 1953), and the linear relationship proposed by Ge et al. (2015) based on clay contents of the sediment samples obtained from the outer regions of the estuary is applied. The τ_{ce} values estimated using the two distinct methods discussed above are integrated in the model and prescribed for the coarsest mud fraction (m4), which ranges from 0.03 to 0.48 N m^{-2}. The τ_{ce} near the boundary of the inner estuary and mouth bar area is smoothed manually. For each of the finer fractions, the τ_{ce} is scaled from the derived spatial distribution of m4 by a factor (<1), depending on the grain size. For all the mud fractions, the erosion parameter M is 5.0×10^{-5} kg m^{-2} s^{-1}, the specific density is 2650 kg m^{-3}, and the dry bed density is 500 kg m^{-3}.

The initial bed composition of the six fractions is based on measurements that were taken in September 2015. However, the resolution of the sampling sites is insufficient for identifying the spatial variations between shoals and channels (Fig. 4). Using the measurements as the initial conditions, a Bed Composition Generation (BCG) run is conducted in advance under mean river discharge for each morphological modeling case. Following the approach of Van der Wegen et al. (2011b), the BCG run is based on bathymetry observed in the first year of each modeling period, and only the bed composition is updated but not the bed-level. Each bed cell consists of an active layer (0.25 m) and an underlayer (6 m), which corresponds with the results presented by Van der Wegen et al. (2011b). The BCG run lasts for one month, and the resulting bed composition shows coherent channel-shoal variability and is applied as the initial conditions in the morphological simulations. The derived bed composition for the 2002-2010 hindcast case, for instance, is shown in Fig. 6. The results show that s1 and m3 are the dominant fractions and that the sand content decreases seaward, which is similar to the observed results (Liu et al., 2010). Fine cohesive sediment mainly accumulated at the mouth of the estuary, which agrees with the field data. An equilibrium concentration of non-cohesive sediment is applied at the open boundaries. The SSC of the cohesive fractions at Datong is assumed to equal only a quarter of the total measured SSC (Table 1).

4. Model validations

4.1 Sensitivity to the morphological factor

The morphological model is validated against morphological changes that occurred during three periods i.e., 1958-1978, 1986-1997, and 2002-2010. In the Delft3D model, no robust and objective method exists for determining the highest MF for a given simulation (Ranasinghe et al., 2011). Van der Wegen and Roelvink (2012) used an MF value of 400 for pattern formation of the Western Scheldt estuary, while Dissanayake et al. (2012) used an MF value of 60 to investigate morphological change in a small bay over a 15-year period. Notably, different sediment formulas were used in these studies. The selection of MF depends on the morphological timescale and relevant behaviour of the system and must be determined according to the modeled processes and model configuration.

According to the river input schematization method described in Section 3.4, the model includes three levels of WD conditions, i.e., high (P4), medium (P2, P3, P5 and P6), and low (P1) (Table 1). A lower MF is applied for the high WD condition to avoid overestimating changes, and a higher MF is used to accelerate the low WD condition. A sensitivity analysis is performed to select an optimal MF. The erosion stage (1986-1997) is chosen as a modeling period for the sensitivity analysis because the evolution pattern during this stage is hardly influenced by human activities (Luan et al., 2016). Four sensitive cases are defined, including a reference case with MF values of 33, 22, and 11 for dry, medium and wet WD conditions, respectively (as shown in Table 1), and three cases with constant MF values of 11, 33 and two times greater than the reference case. The hydrodynamic simulation time of each period in the three cases is modified accordingly, ensuring the same morphological simulation time of the corresponding period among all cases. One additional case is defined which applied the same settings as the reference case except that the six periods are in a different order (P1, P6, P5, P4, P3 and P2), which aims at exploring the mutual influences of each period and their contributions to the differences between the cases. Quantitative comparisons of the erosion and deposition volumes of different MF cases are used to validate model performance. The reference case and the case with MF=11 produce similar erosional and depositional volume changes in the inner estuary, while the cases with MF=33 and MF=two times the reference exhibit large deviations (Fig. 7a). In the mouth bar area, the changes of volume in all cases are highly variable throughout the tidal cycles. The cumulative sediment volume changes in the reference case and when MF=11 also show similar results, although there is a phase difference that may be due to different simulation times (Fig. 7b). The other two cases produce different variations characterized by lower erosional volume. The case with MF=33 results in a slightly greater depositional volume, while the case with MF=two times the reference yields a much lower depositional volume. The sediment volume variations of the additional case show a same phase as the reference case, while the amplitude deviations occur after the second period (P6) and peak in the P4 (Fig. 7). One period represents 1-2 morphological years determined by hydrodynamic simulation times and MF values (Table 1). Therefore morphological changes within one such period are considerable, and they cannot a priori be assumed to be linear and reversible, as is typically assumed with the MF approach. This may explain the differences between the cases with different MF values. The erosion and deposition patterns between the reference case and the case with MF=11 are of negligible difference, while the differences increase with the MF values and become significant in the case with MF=two times the reference, particularly at areas where the modeled bed-level changes are remarkable (not shown here). It is suggested that the sensitivity to MF on the erosion and deposition patterns is consistent with the sediment volume changes. Larger MF values result in larger deviations from the reference case. Therefore, the MF values of the reference case are considered reasonable and are adopted for 1986-1997 hindcast modeling.

Accordingly, the simulation time of each period (P1-P6) is specified (Table 1). The length of each period spans at least 0.5 months and represents a complete neap-spring tidal cycle. The hydrodynamic computation of 6 months produces the specified time span of morphological changes (e.g., 8 years for 2002-2010). Thus, the model results are the summation of the accelerated bed-level changes during the 6 periods (P1-P6) with different combinations of river and sediment discharge instead of the actual successive calendar years. The MF values in other hindcast and forecast simulations are determined in a similar manner using sensitivity simulations (see Table 1). For instance, in the 2002-2010 simulation, the MF values of 8 and 24 are applied for P4 and P1, respectively, and an MF of 16 is applied to the remaining periods. With such model configuration, a standard case takes approximately 3 days when using a 3.2 GHz, 3.43 Gb RAM PC.

4.2 Seasonal variations of flow and sediment transport

The residual current and residual total sediment transport are obtained by averaging the modeled hourly results during the dry (P1) and wet seasons (P4). The results indicate that the variations of river inputs strongly influence residual transport in the Yangtze Estuary. As shown in Fig. 8, the residual patterns of flow and sediment transport during the dry and wet seasons are ebb-dominant due to huge amount of river flow and sediment supply. Residual transport at the shallow shoals is insignificant due to the low current at these areas. High river discharge enhances residual transport, especially in the upstream part of the inner estuary (Fig. 8c, d). The flood channels tend to exhibit ebb-directed residual transport during the wet season. The construction of training walls along the North Passage results in increased flow through the South Passage relative to the North Passage (Dou et al., 2014), which enhances the residual current and sediment transport at the entrance of the South Passage. Strong residual sediment transport occurs at the seaward end of the North and South Passages, which is the present depocenter of the Yangtze Estuary and is a muddy area with high sediment exchange (Liu et al., 2010).

The transport processes of the four mud fractions show distinct features under high and low river discharge. The cumulative fluxes of all the mud fractions in the HS section (see Fig. 1b for the location) are larger in the wet season than in the dry season (Fig. 9), which is primarily attributed to the high WD and greater sediment supply during the wet season (Table 1). The similarity of the fluxes of m1 and m2 fractions in the wet season suggest that the inner estuary behaves more or less as a bypassing conduit for these two fine mud fractions. The low amount of the m4 fraction that is transported through the HS section indicates that deposition of the coarsest fraction occurs in the inner estuary. The cumulative flux of the m3 fraction during both seasons is the largest among the four mud fractions, and the cumulative flux of the m2 fraction exceeds the finest m1 fraction during the dry season (Fig. 9). Both fluxes are subject to bed composition of the inner estuary (Fig. 6c, d).

4.3 Results

4.3.1 Erosion and deposition patterns

Fig. 10 shows the modeled and observed erosion and deposition patterns for the 1958-1978, 1986-1997 and 2002-2010 periods. Visual comparisons indicate that the modeled patterns of the morphological changes during the three periods qualitatively agree with the observations. The evolution of the inner estuary was characterized by channel migration and sand bar accretion and movement, whereas the mouth bar area primarily featured accretion on shallow tidal flats and erosion in the main channels, which corresponds with the field data (Luan et al., 2016). The comparisons of the evolution patterns of the inner estuary show better results than the comparisons of the mouth bar area for all three hindcast cases. Moreover, among the hindcast cases, the 2002-2010 hindcast case provides the best agreement with the overall patterns.

In the 2002-2010 hindcast case, erosion along the main channel within the inner estuary is approximately reproduced although the deposition on the seaward margin of the lower Biandan Shoal is underestimated (Fig. 10a, b). In the mouth bar area, accretion occurred at the seaward portion of the East Chongming mudflat, East Hengsha Shoal, Jiuduansha Shoal and the dike-sheltered areas within the North Passage, which are all well captured by the model (Fig. 10a). The deposition volumes in the northern and southern dike-sheltered areas are underestimated and overestimated, respectively, possibly due to the discontinuous construction processes of the twin jetties and the series of perpendicular groins. Continuous dredging operations were conducted to maintain the navigation channel depth, and the total dredging amount in 2002-2010 was 386 Mm^3 (Luan et al., 2016). The dredging material were temporally dumped to four sites located on the north side of the upstream North Passage. Nearly 14.5 Mm^3 of the dumped mud are lost from the sites between 2006.9 and 2008.12 (YEWAB, 2008), which could provide abundant sediment for high deposition in the adjacent dike-sheltered areas. However, dredging and dumping are not included in the model due to the irregular dredging operations and unavailability of detailed dredging data in this hindcast period. This can explain the underestimation of the deposition in the northern dike-sheltered areas. The presence of training walls induces enhanced erosion in the middle section of the North Passage and at the entrance of the South Passage (Fig. 10a), where the gradient of residual sediment transport is large (Fig. 8b, d). The model results show intensive erosion at seaward side of the North Passage and South Passage, which was also observed (Fig. 10a).

The 1986-1997 and 1958-1978 hindcast cases also show reasonable results (Fig. 10c-f). For the inner estuary, the modeled patterns resemble the erosion-dominant pattern in 1986-1997 and the deposition-dominant pattern in 1958-1978 (Fig. 10c, e). The erosional conditions are probably attributable to river flooding, while the depositional conditions are attributable to a massive riverine sediment supply (Luan et al., 2016). In contrast, the evolution patterns of the mouth bar area show relatively poor model performance. Specifically, the model overestimates erosion along the main channels in both hindcast periods and accretion at shallow shoals in 1958-1997. Several reasons are responsible for the deviations and will be discussed in Section 6.3. Overall, the model qualitatively reproduced the erosion and deposition patterns for three hindcast periods.

4.3.2 Sediment volume changes

Model performance is quantitatively assessed by comparing changes in sediment volume. Fig. 11 shows the modeled erosion, deposition and net sediment volume changes of the inner estuary and mouth bar area for three hindcast cases and their comparison with measured values. All the hindcast cases reproduce net deposition or erosion in the two areas, indicating that the sediment gains and losses in the study area are qualitatively captured by the model. The erosion volume in the inner estuary is also reproduced by the model better than the mouth bar area. The model performance is best for the most recent period. In the 2002-2010 hindcast case, net erosion and net deposition occur in the inner estuary and mouth bar area, respectively. In this case, the model yields a lower deposition volume within the inner estuary, which leads to the overestimation of the net erosion volume. Meanwhile, the net deposition volume in the mouth bar area is slightly underestimated due to excessive erosion in the simulation (Fig. 11a, b). In the 1986-1997 and 1958-1978 hindcast cases, both the erosion and deposition volumes in the mouth bar area are overestimated and less accurate that the net changes of erosion and deposition (Fig. 11c-f). Large erosion and deposition volumes are reflected by drastic bed-level changes (Fig. 10c, e), which could result from the application of uniform sediment parameters and inaccurate bed compositions in these two hindcast cases. Meanwhile, the modeled volume changes in the inner estuary are similar to the observed changes, and greater deposition in 1958-1978 results in the overestimation of the net change. The sediment volume changes quantitatively demonstrate the reliability of the morphological model.

4.3.3 Hypsometry curves

A hypsometry curve describes the relationship between the horizontal water surface area and the water depth below a reference datum (mean sea level in this study) and provides information on the vertical geometry of the full depth range. As shown in Fig. 12, the agreement decreases gradually from the most recent hindcast period to the earliest hindcast period, which is consistence with comparisons of evolution patterns and sediment volume changes. The comparison between the hypsometry curves of the inner estuary in 2002 and 2010 indicates accretion at shallow sand bars (>–5 m), erosion in deep channels (<–10 m), and minor changes in other depth ranges (between –5 m and –10 m) (Fig. 12a). The 2002-2010 hindcast captures these features, although more erosion is modeled in deeper areas. In the mouth bar area, the dividing depth for accretion and erosion is approximately –8 m, which is reproduced well by the model with only a slight overestimation of erosion (Fig. 12b). In 1986-1997, erosion of the inner estuary is primarily between –20 m and –5 m. The hindcast modeling reproduces erosion in the deep area, and more deposition occurs at the shallow area (Fig. 12c). Minor changes were observed in the hypsometry curve of the mouth bar area during this period, with only slight accretion above –5 m. Accretion at shallow shoals and erosion along the channel are overestimated by the model (Fig. 12d). The 1958-1978 hindcast case shows limited model skill, which is reflected by excessive deposition and erosion (Fig. 12e, f). Nevertheless, the hypsometry comparisons show good performance, especially for the latest period.

Overall, the validation of the morphological model based on erosion/deposition patterns, sediment volume changes and hypsometry curves demonstrates the model has relatively high qualitative and quantitative forecasting abilities for evolution trends over the next 2 decades. The model forecast scenarios and results are described in the following section.

5. Model forecast

5.1 Scenario settings

The morphological evolution for 2010-2030 is forecasted considering RSLR and different WD and SSD conditions by applying the same sediment parameters as the 2002-2010 hindcast case. Previous studies suggested that the RSLR by 2030 would be 0.112 m due to rapid sea-level rise and land subsidence in the Yangtze Estuary (Wang et al., 2012; Qiu, 2014). Yang et al. (2010) analyzed the monthly WD data between 1950 and 2008 and identified an increasing trend in January and February and a decreasing trend from August to November. The Three Gorges Dam and the South-to-North Water Diversion Project, which are among the largest human projects within the river basin, influence the seasonal WD trends. By 2050, the South-to-North Water Diversion Project will result in a mean WD decrease of approximately 4.8% (Yang et al., 2010). Considering the combined impacts of climate change and human activities, the WD during the dry season (P1) in 2030 is 13057 $m^3 s^{-1}$ (according to Qiu (2014)). The WDs of P5 and P6 are scaled based on a 2.5% reduction in the annual WD by 2030. The other periods (P2-P4) use the same WD as the 2002-2010 hindcast case. During the first decade since the operation of the Three Gorges Dam in 2003, the annual mean SSD has decreased to ~150 Mt yr^{-1} (Yang et al., 2014), and were as low as 85 and 72 Mt yr^{-1} in the drought years of 2006 and 2011, respectively. Integrating various factors from all reaches of the river, Yang et al. (2014) predicted that the SSD would decrease to ~120 Mt yr^{-1} by the 2020s and to ~110 Mt yr^{-1} by the 2050s, and would unlikely fall below 100 Mt yr^{-1} before 2050 (Yang et al., 2007). Here, six scenarios are designed to forecast the evolution trends through 2030 (Table 3). Scenario 0 applies the WD of the 2002-2010 hindcast case and an annual SSD of 150 Mt yr^{-1} without RSLR, which represent the current river input conditions. Based on Scenario 0, Scenario 1 considers the RSLR and Scenario 2 applies an annual SSD of 125 Mt yr^{-1}. The WD predicted for 2030 and RSLR are applied in all other scenarios. Scenarios 3, 4 and 5, with SSDs of 150, 125 and 100 Mt yr^{-1}, respectively, represent the current, most likely and extremely low riverine sediment supplies, respectively. The annual distribution of the SSD in all scenarios is consistent with the recent hindcast period. Thus the SSDs for the periods (P1-P6) are determined by scaling the SSDs of the hindcast 2002-2010 case according to the ratio of the annual SSD of the forecast scenario to 169 Mt yr^{-1} (Table 1). Hence, the SSCs of the periods (P1-P6) are obtained and prescribed at Datong. The annual SSCs of Scenarios 0-5 are 0.174, 0.174, 0.145, 0.179, 0.149 and 0.119 kg m^{-3}, respectively (Table 3).

5.2 Evolution trend through 2030

The predicted erosion/deposition patterns of all the scenarios visually resemble each other. Therefore, only Scenario 4, which considers the most likely future conditions is shown (Fig. 13a). The entire estuary is characterized by erosion, with deposition only occurring in a few areas. The main channels, including the South Branch (both ebb and flood channels) and the North Channel, continue to be eroded, which is increasing the depths of the channels within the inner estuary. Accretion occurs at the margins of the shoals, such as at the head of the Baimao Shoal, the seaward end of the Biandan Shoal and the head of the Zhongyang Shoal. Several connecting channels form on the Biandan and Zhongyang Shoals. Deposition also occurs along the southern bank of the South Branch and along the middle sand bar in the South Channel. Erosion occurs at both ends of the South Passage due to the presence of submerged dikes and reduced sediment supply. Deposition continues in the dike-sheltered areas in the North Passage, which results in further narrowing of the channel. The four intertidal flats at the delta front exhibit distinct evolution trends (Fig. 13a). Specifically, the East Chongming mudflat suffers from overall erosion, which is reflected by the retreat of the 5 m isobath. Notably, erosion leads to the development of a tidal channel on the southern East Chongming mudflat and a new bifurcation. The East Hengsha Shoal is characterized by accretion and the southeastward extension of the 5 m isobath; however the east side of Hengsha Shoal is slight retreating. Minor changes occur at Jiuduansha Shoal except for erosion at the seaward end along the jetty. At East Nanhui, a small flood channel emerges that is aligned with the direction of tidal propagation. The statistical analysis of the sediment volume changes in Scenario 4 indicates that the inner estuary experiences net erosion, and the mouth bar area shifts from net accretion during 2002-2010 to net erosion by 2030 (Fig. 14).

The erosion and deposition intensities, but not the spatial evolution patterns, differs between the future scenarios. The differences of morphological evolution between Scenarios 1 and 0 are primarily found in the mouth bar area, especially in its northern part, reflected by more deposition in Scenario 1 with RSLR (Fig. 13b). The sediment volume changes of the inner estuary in Scenarios 1 and 0 are nearly the same, while less erosion and more deposition volumes of the mouth bar area are produced in Scenario 1 relative to Scenario 0, leading to reduced net erosion volume when considering RSLR (Fig. 14). The morphological changes in Scenarios 3 and 1 are slightly different only with respect to more deposition in the inner estuary in Scenario 3 (Fig. 13d), suggesting that the effects of the changing WD on the morphological evolution of the Yangtze Estuary are limited over the next 2 decades. However, decreasing SSD will accelerate erosion across the entire estuary whether or not the RLSR is considered (Fig. 13c, e). Comparing the sediment volume changes between Scenarios 2 and 4 indicated that the RSLR can partly compensate the net erosion in the mouth bar area if the effects of WD change are ignored (Fig. 14). Erosion will be considerable under conditions of extremely low sediment supply, especially in the inner estuary (Fig. 13f). A low sediment supply will increase the erosion volume, decrease the deposition volume and, subsequently, enhance the net sediment loss (Fig. 14). Notably, all scenarios show net erosion trend in both the inner estuary and mouth bar area (Fig. 14).

6. Discussion

6.1 Effects of high river discharge

Generally, estuarine morphodynamics are the accumulated results of tidally averaged residual sediment transport and its gradients (Roelvink and Reniers, 2011; Guo et al., 2014). High river inputs (river flow and fine sediment) and the interactions of river inputs with tidal currents are regarded as the primary factors that govern the morphological evolution of the Yangtze Estuary (Chen et al., 1985; Yun, 2004). The river-tide dynamics of the Yangtze Estuary are characterized by a transition from fluvial-dominant to tidal-dominant conditions along the tidal channel downstream of Datong (Guo et al., 2015b; Zhang et al., 2016). River flow causes along-channel tidal decay by damping the tidal amplitude and dissipating the tidal energy (Jay and Flinchem, 1997). Our model captured this feature and reproduced the M2 tidal amplitude variations and water levels during the wet and dry seasons (Supplementary Fig. S3, online). For the estuarine area downstream of Xuliujing, this transition is still apparent, as reflected by the flow patterns (Fig. 8a, c) and bed sediment grain size distribution (Liu et al., 2010). River flow flushes fine sediment to the river mouth and enhances ebb-directed residual current and sediment transport (Guo et al., 2014), particularly during the wet season. The enhancement of residual current and sediment transport by high river discharge is more remarkable in the inner estuary than in the mouth bar area (Fig. 8c, d). A large residual sediment transport gradient results in major erosion along the main channel of the South Branch and North Channel during the wet season (Fig. 10a). Notably, the cumulative flux of the finest fraction (m1) through the HS section is slightly larger than the cumulative flux of the coarser fraction (m2) during the wet season, which is different from the trend that occurs during the dry season. Possible explanations for this difference include that a high river discharge induces a relatively higher capacity of the m1 fraction and that more of the m1 fraction (relative to the coarser fraction) is eroded from the inner estuary. This excessive erosion is considered as evidence of river dominance, which was also found in the long-term morphodynamic modeling of a schematized fluvio-deltaic system with a landform comparable to that of the Yangtze Estuary (Guo et al., 2015c). An extremely high river discharge may even induce erosion in the mouth bar area. For instance, the formation of the North Passage in 1954 and the East Hengsha Connecting Channel in 1973 were the consequences of extreme river floods (Yun et al., 2004). Therefore, it can be concluded that high river discharge can influence the river-tide dynamics by leading to seaward extension of the fluvial-marine transition interface and subsequent morphological changes.

6.2 Implications for the coming decades

The data analysis suggests that the inner estuary switched from net deposition to net erosion in the 1980s, while the mouth bar area experienced continuous net accretion during the past half century despite the decreasing sediment input from the river (Luan et al., 2016). The results of the forecast simulations in this study indicate that both the inner estuary and mouth bar area will undergo net erosion by 2030 (Fig. 14) due to river sediment reduction, RSLR and the current configuration of estuarine engineering projects. Thus, the inner estuary will be continuously eroded, while the mouth bar area begins to experience net erosion in the next two decades, primarily due to the low fluvial sediment supply. Net erosion is also predicted to occur in the mouth bar area under the present SSD conditions (Scenario 3). This prediction can be partly explained by the decreased deposition rate in the dike-sheltered areas and the slow (or even reversed) tidal flat extension due to land reclamation at East Hengsha and East Nanhui. In the forecast modeling, the inner estuary shows an erosion pattern that is similar to that of the last decade, while major erosion within the mouth bar area will occur at the present depocenter and along the main channels (Fig. 13a). Erosion will also occur on the tidal flats, which may lead to unexpected consequences. For instance, the formation of a secondary tidal channel at East Chongming mudflat may cause more saltwater intrusion through the North Channel and threaten freshwater accessibility in the Qingcaosha Reservoir (Li et al., 2014), which currently supplies >50% of the total freshwater to Shanghai. Additionally, erosion of the seaward Jiuduansha Shoal and the formation of a flood channel may affect the stability of the nearby jetty.

Previous studies suggested that RSLR can enhance tidal energy, and hence bed shear stress leading to erosion, and also decrease energy slope leading to deposition (Canestrelli et al., 2010). The above two counteracting effects determine the morphological effects of RSLR, depending on the amount the fluvial sediment supply and delta configuration. Model results in this study indicate that the RSLR favors deposition in the mouth bar area under both present and future decreased SSD conditions (Fig. 13b, 14). Possible reasons are that both riverine sediment and eroded sediment of the inner estuary is delivered to the mouth bar area, and that the enhancement of tidal flushing by RSLR is insignificant compared with huge amount of WD, and therefore the increased water depth provides more chances for sediment deposition during slack waters. The inner estuary is less sensitive to the RSLR due to its strong ebb-dominance. The RSLR-induced deposition also reflects the resilience of the Yangtze Estuary to increasing sea level (Ganju and Schoellhamer, 2010). Model-based study on the response of Fly River to Pleistocene-Holocene sea-level rise by Parker et al. (2008) indicated that sea-level rise could trigger net deposition at the millennial timescale, and highlighted the significance of the sufficiency of sediment supply on delta extension under sea-level variation.

Changes in WD only result in negligible differences in morphological changes (Fig. 13d) because the amplitude of change is relatively small compared to the absolute magnitude of the river discharge. Although river discharge plays important roles in flushing riverine sediment and enhancing ebb residual transport, the predicted changes of the annual amount and seasonality of the WD cannot induce substantial morphological responses within the Yangtze

Estuary. A decrease in the river sediment supply from the present amount of 150 Mt yr^{-1} to 100 Mt yr^{-1} will result in continuous erosion, which is independent on the RSLR and WD change (Fig. 13c, e, f). It implies that the decrease of SSD is the key factor determining the erosion trend in the next 2 decades. This raises a question regarding the erosion limits of the mouth bar area and the subaqueous depocenter. Stratigraphic analysis of sediment cores from the Yangtze delta has indicated that the thickness of the Holocene layer around the estuary ranges from 10 m to 46 m and that the maximum thickness coincides with the mouth bar area (Stanley and Chen, 1993; Liu et al. 2007). These modern deposits are usually erodible, suggesting that the availability of sediment from the estuarine bed is not a limiting factor for erosion at decadal or centennial timescales. It is assumed that the combined effects of the decreased erosion capacity that results from increasing bed depth and erosion resistance due to compaction and consolidation could be used to determine the morphological equilibrium status of the Yangtze Estuary. The timescale required to achieve the equilibrium is unknown and merits future study.

6.3 Model efficacy

The process-based morphodynamic modeling approach applied in this study shows significant value for numerically reproducing decadal morphological processes and forecasting the future evolution trends of the large-scale Yangtze Estuary. The promising performance of this present model is largely attributed to the inclusion of variations in river inputs and multiple sediment fractions. Model parameters related to sediment are based on field samples collected in the Yangtze Estuary (Fig. 4) and consequently represent reality. The distinct behaviors of the four mud fractions during the dry and wet seasons also facilitate our understanding of their effects on morphological changes. Hindcast modeling without the above factors does not produce reasonable results, demonstrating the necessity of considering these factors to obtain adequate predictions. The good performances of the hindcast simulations demonstrate that our model reliably predicts evolution trends at a decadal timescale and can provide valuable information for the sustainable management of the Yangtze Estuary.

The latest hindcast case (2002-2010) shows the best model performance. This is probably because the initial bed compositions of all the hindcast simulations are derived through BCG runs based on sediment samples obtained in September 2015 (Fig. 4, 5), which are more representative for the recent hindcast period than for earlier periods. This choice is a compromise because few bed composition data were obtained from the Yangtze Estuary before the 1990s. The bed composition during 1958-1978 is likely different from the current bed composition since that the composition of riverine sediment supply has changed (Yang et al., 2014). Another reason is that the older hindcast periods are longer than the recent period (2002-2010), and the deviations may accumulate along with the morphological simulation time, particularly with larger MF values in older periods. Meanwhile, strong deposition and significant changes of channel-shoal pattern were observed in 1958-1978 (Luan et al., 2016), which could increase the difficulty for morphological hindcast with high accuracy.

Better model performance is achieved for the inner estuary than for the mouth bar area, which may be caused by multiple reasons. Firstly, the mouth bar area is dominated by fine cohesive sediment with a wide grain size range. Currently, the morphological modeling considering cohesive sediment dynamics is less developed than that of non-cohesive sediment.

The model results indicate that morphological modeling of the mouth bar area requires more accurate sediment parameters than that of the inner estuary. Secondly, numerical experiments by Canestrelli et al. (2014b) have demonstrated that frictional effects play an important role on morphodynamics of river mouth bars by influencing jet instability. Present model applies constant Manning coefficient of 0.015 at the mouth bar area after calibrations of tides and hydrodynamics (Supplementary material, online), which is comparable with the values used by Hu et al. (2009) and Kuang et al. (2013). The river jets from the North and South Channel debouch into the three main channels within the mouth bar area. The channel widths and depths are 5-10 km and 5-10 m, respectively. Following the method proposed by Canestrelli et al. (2014b), the jet stability number is calculated in the range of 0.51-2.58. This range obviously lies in the stable area of a stability diagram deduced by Canestrelli et al. (2014b). The large stability number is primarily due to the much larger channel width relative to the depth and favors mouth bar formations, i.e. deposition in the main channels within the mouth bar area. However, excess erosion along the main channels is produced by the hindcast simulations. This is probably because that the simplified modeling framework of Canestrelli et al. (2014b) ignores the prevailing forcings (e.g. seasonal river flow, tides) and thereby is less representative to the Yangtze Estuary. It seems that the frictional effects on the model performance of mouth bar area are limited relative to the dominant external forcings. Thirdly, the model reproduces the depth-averaged flow and sediment transport patterns well, which are responsible for the morphological evolution in the inner estuary. In contrast, the mouth bar area, which coincides with the estuarine turbidity maximum, is subject to more complicated processes, including density stratification, gravitational circulation, sediment resuspension and flocculation (Wu et al., 2012). High SSC (>10 kg m^{-3}) near the bottom can be generated due to sediment trapping and intensive water-bed exchange, and can be enhanced by suppression of turbulence due to vertical density gradients. Field observations and model studies indicated that these 3D processes had likely induced severe deposition in the dredged navigation channel along the North Passage (Liu et al., 2011; Wan et al., 2014). Our model excludes vertical flow and sediment transport variations and is unable to reproduce stratification and near-bed sediment trapping, which could systematically lead to overestimation of seaward transport and thus underestimation of deposition in the estuary. This may partly explain the strong erosion along the channels within the mouth bar area (Fig. 10a, c, e). To what extent a 3D model can improve these results remains unknown and deserves further investigations. Other processes that are not considered in the model include the variation of the sediment fraction compositions at Datong and the occurrence of storm events. Van der Wegen et al. (2011) argued that increasing model complexity does not necessarily lead to better model performance due to model limitations associated with more advanced process descriptions and the increased difficulty of interpreting model results. This study suggests that the considered depth-averaged model is capable of modeling the morphodynamics of the Yangtze Estuary at a decadal timescale.

Peak WD and SSD values during flood events are not considered in our model for simplicity. When studying the Yangtze Estuary, Yun (2004) estimated that a discharge of 60,000 m^3 s^{-1} (or channel-forming discharge) can induce significant morphological changes. Peak SSDs usually occur together with the peak WDs during the wet season. For instance, the sediment flux at Datong during the 2.5-month flood season in 1998 was estimated to equal

450 million tons (Xu et al., 2005), which is approximately 3 times the current annual sediment flux. Peak flood discharges play an important role in morphological changes. The WD and SSD values applied in the present model are monthly averaged values that are lower than the values observed during peak flood stages. In the most recent decade, erosion of the subaqueous delta and present depocenter has been observed (Fig. 10b). A recent study indicates that eroded sediment can be transported back to the estuary as a new sediment source for accretion (Zhu et al., 2016). However, the factors responsible for the formation of the erosion zone and relevant processes at the intra-tidal to decadal timescales remain poorly understood. The process-based approach in this study can provide a basis for answering these questions.

7. Conclusions

We hindcasted and forecasted the morphological evolution of the large-scale Yangtze Estuary at a decadal timescale by using the process-based Delft3D model system. The Delft3D model considers variations in river inputs and multiple sediment fractions. The morphological model is validated against the evolution observed during three historical periods with distinct evolution processes, i.e., an accretion period (1958-1978), an erosion period (1986-1997) and a recent accretion period with human activities (2002-2010). The modeled erosion and deposition patterns of the three periods agree well with the observations. A statistical analysis of changes in the sediment volume shows that all of the hindcast cases reproduce the net deposition or erosion occurring in the inner estuary and mouth bar area despite small deviations. Comparisons of hypsometry curves also show reasonable results.

Overall, the model performed well for forecasting.

Simulations under future WD and SSD conditions and RSLR provide the evolution trends of the Yangtze Estuary by 2030. Model predictions indicate that both the inner estuary and mouth bar area will experience net erosion by 2030, primarily due to low levels of sediment supply. The evolution patterns within the inner estuary are similar to those during the last decade, while regional erosion in the mouth bar area merits additional management attention, i.e., the deepening of the tidal channel at East Chongming mudflat and the formation of a flood channel on the seaward side of Jiuduansha Shoal. Forecast modeling can provide valuable information about future evolution trends and guide the sustainable management of the Yangtze Estuary. Furthermore, the process-based approach applied in this study can be used to investigate morphological issues in the Yangtze Estuary, such as the morphological effects of peak flood discharge and the formation of the erosion zone at the subaqueous delta.

Acknowledgments

This study is jointly funded by the National Science Foundation of China (41476076, 51320105005 and 41306080) and the project 'Effects of human activities on the eco-morphological evolution of rivers and estuaries' (2008DFB90240) within the Programme of Strategic Scientific Alliance between China and the Netherlands (PSA). Mr. Yang W.L., Dao F.H. and Ji C.L. are thanked for their assistance with field sampling in September 2015. Discussion with Dr. Guo L.C. improved the manuscript. The revision of this paper benefited from the Editor and two anonymous reviewers who provided thoughtful and constructive

comments and suggestions.

Appendix A. Supplementary material

Supplementary material to this article can be found online.

References

Anthony, E.J., Brunier, G., Besset, M., Goichot, M., Dussouillez, P., Nguyen, V.L., 2015. Linking rapid erosion of the Mekong River delta to human activities. Sci. Rep. 5, 14745.

Bagnold, R.A., 1966. An approach to the sediment transport problem from general physics. U.S. Geol. Surv. Prof. Paper 422-I. 37 pp.

Blott, S.J., Pye, K., van der Wal, D., Neal, A., 2006. Long-term morphological change and its causes in the Mersey Estuary, NW England. Geomorphology 81, 185-206.

Bolla Pittaluga, M., Tambroni, N., Canestrelli, A., Slingerland, R., Lanzoni, S., Seminara, G., 2015. Where river and tide meet: The morphodynamic equilibrium of alluvial estuaries. Journal of Geophysical Research: Earth Surface 120, 75-94.

Cameron, W. M., D. W. Pritchard, 1963. Estuaries. In M. N. Hill (ed.), The Sea, Vol. 2. John Wiley & Sons, New York, pp. 306-324.

Canestrelli, A., Fagherazzi, S., Defina, A., Lanzoni, S., 2010. Tidal hydrodynamics and erosional power in the Fly River delta, Papua New Guinea. Journal of Geophysical Research: Earth Surface 115, F4033.

Canestrelli, A., Lanzoni, S., Fagherazzi, S., 2014a. One-dimensional numerical modeling of the long-term morphodynamic evolution of a tidally-dominated estuary: The Lower Fly

River (Papua New Guinea). Sediment. Geol. 301, 107-119.

Canestrelli, A., Nardin, W., Edmonds, D., Fagherazzi, S., Slingerland, R., 2014b. Importance of frictional effects and jet instability on the morphodynamics of river mouth bars and levees. Journal of Geophysical Research: Oceans 119, 509-522.

Chen, J., Zhu, H., Dong, Y., Sun, J., 1985. Development of the Changjiang estuary and its submerged delta. Cont. Shelf Res. 4, 47-56.

Chen, J., Li, D., Chen, B., Hu, F., Zhu, H., Liu, C., 1999. The processes of dynamic sedimentation in the Changjiang Estuary. J. Sea Res. 41, 129-140.

CWRC (Changjiang Water Resources Commission), 2011. Changjiang Sediment Bulletin. (available at:) http://www.cjh.com.cn/pages/nsgb.html (in Chinese).

Dai, Z., Liu, J.T., Fu, G., Xie, H., 2013. A thirteen-year record of bathymetric changes in the North Passage, Changjiang (Yangtze) estuary. Geomorphology 187, 101-107.

Dai, Z., Liu, J.T., Wei, W., Chen, J., 2014. Detection of the Three Gorges Dam influence on the Changjiang (Yangtze River) submerged delta. Sci. Rep. 4, 6600.

Dai, Z., Fagherazzi, S., Mei, X., Chen, J., Meng, Y., 2016. Linking the infilling of the North Branch in the Changjiang (Yangtze) estuary to anthropogenic activities from 1958 to 2013. Mar. Geol. 379, 1-12.

Dalrymple, R.A., Zaitlin, B.A., Boyd, R., 1992. Estuarine facies models: conceptual basis and stratigraphic implications. Journal of Sedimentary Petrology 62, 1130-1146.

Dam, G., van der Wegen, M., Labeur, R.J., Roelvink, D., 2016. Modeling centuries of estuarine morphodynamics in the Western Scheldt estuary. Geophys. Res. Lett. 43, 3839-3847.

Day, J.W., Britsch, L.D., Hawes, S.R., Shaffer, G.P., Reed, D.J., Cahoon, D., 2000. Pattern and process of land loss in the Mississippi Delta: A Spatial and temporal analysis of wetland habitat change. Estuaries 23, 425-438.

Deltares, 2014. User manual Delft3D-Flow: Simulation of multi-dimensional hydrodynamic flows and transport phenomena, including sediments. version 3.15, Delft, Netherlands.

Ding, P.X., Wang, H.J., Meng, X.W., Zhu, J.R., Zhang, L.Q., Shan, X.J., 2016. Evolution trend and vulnerability assessment of typical coastal zones in China under the influence of climate change. Science Press, Beijing, China, pp. 20-40 (in Chinese).

Dissanayake, D.M.P.K., Wurpts, A., Miani, M., Knaack, H., Niemeyer, H.D., Roelvink, J.A., 2012. Modelling morphodynamic response of a tidal basin to an anthropogenic effect: Ley Bay, East Frisian Wadden Sea – applying tidal forcing only and different sediment fractions. Coast. Eng. 67, 14-28.

Dou, R.Q., Guo, W.Y., Ge, J.Z., Ding, P.X., 2014. Analysis for variation of the ebb flow diversion ratios in North Passage of the Yangtze Estuary. J. East China Normal Univ. (Nat. Sci.) 3, 93–104 (in Chinese with English abstract).

Du, P., Ding, P., Hu, K., 2010. Simulation of three-dimensional cohesive sediment transport in Hangzhou Bay, China. Acta Oceanol. Sin. 29, 98-106.

Editorial Board for Marine Atlas, 1992. Marine atlas in Bohai Sea, Yellow Sea and East China Sea (Hydrology). China Ocean Press, Beijing

Gagliano, S.M., Meyer-Arendt, K.J., Wicker, K.M., 1981. Land loss in the Mississippi River Deltaic Plain. Transactions of the Gulf Coast Association of Geological Societies 31, 295-300.

Galloway, W.E., 1975, Process framework for describing the morphologic and stratigraphic evolution of deltaic depositional systems. In: Broussard, M.L. (ed.), Deltas: Models for Exploration. Houston Geological Society, pp. 87-98.

Ganju, N.K., Knowles, N., Schoellhamer, D.H., 2008. Temporal downscaling of decadal sediment load estimates to a daily interval for use in hindcast simulations. J. Hydrol. 349, 512-523.

Ganju, N.K., Schoellhamer, D.H., Jaffe, B.E., 2009. Hindcasting of decadal-timescale estuarine bathymetric change with a tidal-timescale model. Journal of Geophysical Research: Earth Surface 114, F04019.

Ganju, N.K., Schoellhamer, D., 2010. Decadal-timescale estuarine geomorphic change under future scenarios of climate and sediment supply. Estuar. Coast. 33, 15-29.

Ganju, N.K., Jaffe, B.E., Schoellhamer, D.H., 2011. Discontinuous hindcast simulations of estuarine bathymetric change: A case study from Suisun Bay, California. Estuarine, Coastal and Shelf Science 93, 142-150.

Garel, E., Sousa, C., Ferreira, Ó., Morales, J.A., 2014. Decadal morphological response of an ebb-tidal delta and down-drift beach to artificial breaching and inlet stabilisation. Geomorphology 216, 13-25.

Ge, J., Ding, P., Chen, C., Hu, S., Fu, G., Wu, L., 2013. An integrated East China Sea–Changjiang Estuary model system with aim at resolving multi-scale regional–shelf–estuarine dynamics. Ocean Dynam. 63, 881-900.

Ge, J., Shen, F., Guo, W., Chen, C., Ding, P., 2015. Estimation of critical shear stress for erosion in the Changjiang Estuary: A synergy research of observation, GOCI sensing and modeling. Journal of Geophysical Research: Oceans 120, 8439-8465.

Giosan, L., Syvitski, J., Constantinescu, S., Day, J., 2014. Climate change: protect the world's deltas. Nature 516, 31-33.

Guo, L.C., van der Wegen, M., Roelvink, J.A., He, Q., 2013. The tidal channel morphodynamics in the Yangtze Estuary: a case of the South Branch. Proceeding of the 7th International Conference on Coastal Dynamics. Arcachon, France, pp. 781-790.

Guo, L.C., van der Wegen, M., Roelvink, J.A., He, Q., 2014. The role of river flow and tidal asymmetry on 1D estuarine morphodynamics. Journal of Geophysical Research: Earth Surface 119.

Guo, L., van der Wegen, M., Roelvink, D., He, Q., 2015a. Exploration of the impact of seasonal river discharge variations on long-term estuarine morphodynamic behavior. Coast. Eng. 95, 105-116.

Guo, L.C., van der Wegen, M., Jay, D.A., Matte, P., Wang, Z.B., Roelvink, D.J.A., He, Q., 2015b. River-tide dynamics: Exploration of non-stationary and nonlinear tidal behavior in the Yangtze River estuary. Journal of Geophysical Research: Oceans, 120.

Guo, L.C., van der Wegen, M., Roelvink, D.J.A., Wang, Z.B., He, Q., 2015c. Long-term, process-based morphodynamic modeling of a fluvio-deltaic system, part I: The role of river discharge. Cont. Shelf Res. 109, 95-111.

He, Q., Guo, L., Liu, H., & Wang, Y. 2015. Changjiang Estuary Sediment Transport Dynamics. In Ecological Continuum from the Changjiang (Yangtze River) Watersheds to the East China Sea Continental Margin (pp. 47-69). Springer International Publishing.

Hibma, A., de Vriend, H.J., Stive, M.J.F., 2003. Numerical modelling of shoal pattern formation in well-mixed elongated estuaries. Estuar. Coast. Shelf Sci. 57, 981-991.

Hoitink, A.J.F., Hoekstra, P., van Maren, D.S., 2003. Flow asymmetry associated with astronomical tides: Implications for the residual transport of sediment. Journal of Geophysical Research: Oceans 108, 3315.

Hu, K., Ding, P., Zhu, S., Cao, Z., 2000. 2-D Current Field Numerical Simulation Integrating Yangtze Estuary with Hangzhou Bay. China Ocean Engineering (01): 89-102.

Hu, K., Ding, P., Wang, Z., Yang, S., 2009. A 2D/3D hydrodynamic and sediment transport model for the Yangtze Estuary, China. J. Marine Syst. 77, 114-136.

Ikeda, S., 1982. Lateral bed load transport on side slopes. Journal Hydraulics Division ASCE 108, 1369-1373.

Jacobs, W., Le Hir, P., Van Kesteren, W., Cann, P., 2011. Erosion threshold of sand–mud mixtures. Cont. Shelf Res. 31, S14-S25.

Jaffe, B.E., Smith, R.E., Foxgrover, A.C., 2007. Anthropogenic influence on sedimentation and intertidal mudflat change in San Pablo Bay, California: 1856–1983. Estuar. Coast. Shelf Sci. 73, 175-187.

Jay, D.A., Flinchem, E.P., 1997. Interaction of fluctuating river flow with a barotropic tide: A demonstration of wavelet tidal analysis methods. Journal of Geophysical Research: Oceans 102, 5705-5720.

Kuang, C. et al., 2013. Numerical prediction of medium-term tidal flat evolution in the Yangtze Estuary: Impacts of the Three Gorges project. Cont. Shelf Res. 52, 12-26.

Lesser, G.R., Roelvink, J.A., van Kester, J.A.T.M., Stelling, G.S., 2004. Development and validation of a three-dimensional morphological model. Coast. Eng. 51, 883-915.

Lesser, G.R., 2009. An approach to medium-term coastal morphological modeling. Doctoral Thesis. Department of Civil Engineering, Delft University of Technology, Delft, The Netherlands.

Li, J., Zhang, C., 1998. Sediment resuspension and implications for turbidity maximum in the Changjiang Estuary. Mar. Geol. 148, 117-124.

Li, L., Zhu, J., Wu, H., Guo, Z., 2014. Lateral Saltwater Intrusion in the North Channel of the Changjiang Estuary. Estuar. Coast. 37, 36-55.

Li, X., Liu, J.P., Tian, B., 2016. Evolution of the Jiuduansha wetland and the impact of navigation works in the Yangtze Estuary, China. Geomorphology 253, 328-339.

Liu, G., Zhu, J., Wang, Y., Wu, H., Wu, J., 2011. Tripod measured residual currents and sediment flux: Impacts on the silting of the Deepwater Navigation Channel in the Changjiang Estuary. Estuar. Coast. Shelf Sci. 93, 192-201.

Liu, H., He, Q., Wang, Z., Weltje, G.J., Zhang, J., 2010. Dynamics and spatial variability of near-bottom sediment exchange in the Yangtze Estuary, China. Estuar. Coast. Shelf Sci. 86, 322-330.

Liu, J.P., Xu, K.H., Li, A.C., Milliman, J.D., Velozzi, D.M., Xiao, S.B., Yang, Z.S., 2007. Flux and fate of Yangtze River sediment delivered to the East China Sea. Geomorphology 85, 208-224.

Luan, H.L., Ding, P.X., Wang, Z.B., Ge, J.Z., Yang, S.L., 2016. Decadal morphological evolution of the Yangtze Estuary in response to river input changes and estuarine engineering projects. Geomorphology 265, 12-23.

McCann, D., 2011.Long-term Morphological Modeling of Tidal Basins (PhD. Dissertation)

Bangor University, Bangor, UK.

Milliman, J.D., 1997. Blessed dams or damned dams? Nature 386, 325-327.

Orton, G.J., Reading, H.G., 1993. Variability of deltaic processes in terms of sediment supply, with particular emphasis on grain size. Sedimentology 40, 475-512.

Pan, L., Ding, P., Ge, J., 2012. Impacts of Deep Waterway Project on Morphological Changes within the North Passage of the Changjiang Estuary, China. J. Coastal Res., 1165-1176.

Parker, G., Muto, T., Akamatsu, Y., Dietrich, W.E., Lauer, J.W., 2008. Unravelling the conundrum of river response to rising sea-level from laboratory to field. Part II. The Fly–Strickland River system, Papua New Guinea. Sedimentology 55, 1657-1686.

Partheniades, E. 1965, Erosion and deposition of cohesive soils, J. Hydraul. Division, ASCE, 91(1), 105-139

Qiu, C., 2014. The responses of saltwater intrusion to climate change and major projects in the Changjiang River Estuary. PhD thesis, East China Normal University (In Chinese).

Ranasinghe, R., Swinkels, C., Luijendijk, A., Roelvink, D., Bosboom, J., Stive, M., Walstra, D., 2011. Morphodynamic upscaling with the MORFAC approach: Dependencies and sensitivities. Coast. Eng. 58, 806-811.

Roelvink, J.A., 2006. Coastal morphodynamic evolution techniques. Coast. Eng. 53, 277-287.

Roelvink J.A., Reniers A.J.H.M., 2011. A guide to coastal morphology modeling. Advances in Coastal and Ocean Engineering. World Scientific.

Shen, H.T., Li, J.F., Zhu, H.F., Zhou, F.G., 1986. Transport of the suspended sediments in the Changjiang Estuary. Journal of sediment research, (01): 1-13 (in Chinese with English abstract).

Skempton, A.W., 1965. The colloidal activity of clay. In: Proceedings of the Third International Conference on Soil Mechanics and Foundation Engineering, vol. I, pp. 57-61.

Smerdon, E.T., Beasley, R.P., 1959. The tractive force theory applied to stability of open channels in cohesive soil. Agricultural Experimental Stability Research Bulletin 715, 1-36.

Song, D., Wang, X.H., Cao, Z., Guan, W., 2013. Suspended sediment transport in the Deepwater Navigation Channel, Yangtze River Estuary, China, in the dry season 2009: 1. Observations over spring and neap tidal cycles. Journal of Geophysical Research: Oceans 118, 5555-5567.

Stanley, D.J., Chen, Z., 1993. Yangtze delta, eastern China: 1. Geometry and subsidence of Holocene depocenter. Mar. Geol. 112, 1-11.

Stanley, D.J., 1996. Nile delta: extreme case of sediment entrapment on a delta plain and consequent coastal land loss. Mar. Geol. 129, 189-195.

Syvitski, J.P.M., Saito, Y., 2007. Morphodynamics of deltas under the influence of humans. Global Planet. Change 57, 261-282.

Syvitski, J.P.M., 2008. Deltas at risk. Sustain. Sci. 3, 23-32.

Syvitski, J.P.M., Kettner, A.J., Overeem, I., Hutton, E.W.H., Hannon, M.T., Brakenridge, G.R., Day, J., Vorosmarty, C., Saito, Y., Giosan, L., Nicholls, R.J., 2009. Sinking deltas due to human activities. Nat. Geosci. 2, 681-686.

Tessler, Z.D., Vörösmarty, C.J., Grossberg, M., Gladkova, I., Aizenman, H., Syvitski, J.P.M., Foufoula-Georgiou, E., 2015. Profiling risk and sustainability in coastal deltas of the world. Science 349, 638-643.

Torfs, H., 1995. Erosion of mud/sand mixtures. Ph.D. Thesis. Katholieke Universiteit Leuven.

Van der Wal, D., Pye, K., Neal, A., 2002. Long-term morphological change in the Ribble Estuary, northwest England. Mar. Geol. 189, 249-266.

Van der Wegen, M., Roelvink, J.A., 2008. Long-term morphodynamic evolution of a tidal embayment using a two-dimensional, process-based model. Journal of Geophysical Research: Oceans 113, C3016.

Van der Wegen, M., Jaffe, B.E., Roelvink, J.A., 2011a. Process-based, morphodynamic hindcast of decadal deposition patterns in San Pablo Bay, California, 1856–1887. Journal of Geophysical Research: Earth Surface 116, F2008.

Van der Wegen, M., Dastgheib, A., Jaffe, B., Roelvink, D., 2011b. Bed composition generation for morphodynamic modeling: case study of San Pablo Bay in California, USA. Ocean Dynam. 61, 173-186.

Van der Wegen, M., Roelvink, J.A., 2012. Reproduction of estuarine bathymetry by means of a process-based model: Western Scheldt case study, the Netherlands. Geomorphology 179, 152-167.

Van der Wegen, M., Jaffe, B.E., 2014. Processes governing decadal-scale depositional narrowing of the major tidal channel in San Pablo Bay, California, USA. Journal of Geophysical Research: Earth Surface 119, 2013J-2824J.

Van Rijn, L.C., 1993. Principles of sediment transport in rivers, estuaries and coastal seas. AQUA Publications, the Netherlands, p. 535.

Walling, D.E., Fang, D., 2003. Recent trends in the suspended sediment loads of the world's rivers. Global Planet. Change 39, 111-126.

Wan, Y., Roelvink, D., Li, W., Qi, D., Gu, F., 2014. Observation and modeling of the storm-induced fluid mud dynamics in a muddy-estuarine navigational channel. Geomorphology 217, 23-36.

Wang, J., Gao, W., Xu, S., Yu, L., 2012. Evaluation of the combined risk of sea level rise, land subsidence, and storm surges on the coastal areas of Shanghai, China. Climatic Change 115, 537-558.

Wang, Y., Dong, P., Oguchi, T., Chen, S., Shen, H., 2013. Long-term (1842–2006) morphological change and equilibrium state of the Changjiang (Yangtze) Estuary, China. Cont. Shelf Res. 56, 71-81.

Wang, Y., Wang, C., Tang, L., Liu, D., Guo, C., Liu, C., Zhao, H., 2014. Long-term morphological response to dredging including cut-across-shoal in a tidal channel-shoal system. Ocean Dynam. 64, 1831-1843.

Warner, J.C., Sherwood, C.R., Signell, R.P., Harris, C.K., Arango, H.G., 2008. Development of a three-dimensional, regional, coupled wave, current, and sediment-transport model. Comput. Geosci. 34, 1284-1306.

Wei, W., Mei, X., Dai, Z., Tang, Z., 2016. Recent morphodynamic evolution of the largest uninhibited island in the Yangtze (Changjiang) estuary during 1998–2014: Influence of the anthropogenic interference. Cont. Shelf Res. 124, 83-94.

Wei, X., Wu, C., 2014. Long-term process-based morphodynamic modeling of the Pearl River Delta. Ocean Dynam. 64, 1753-1765.

Winterwerp, J.C., 2007. On the sedimentation rate of cohesive sediment, in: Maa, J., Sanford, L., Schoellhamer, D. (Eds.), Estuarine and Coastal Fine Sediments Dynamics INTERCOH 2003. Elsevier, pp. 209-226.

Woodroffe, C., Nicholls, R., Saito, Y., Chen, Z., Goodbred, S., 2006. Landscape variability and the response of Asian megadeltas to environmental change. In: Harvey, N. (Ed.), Coastal Systems and Continental Margins. Springer, Netherlands, pp. 277-314.

WUHEE (Wuhan University of Hydraulic and Electric Engineering), 1960. River Hydraulics. China Industry Press. Beijing, China, pp. 13-21 (in Chinese).

Wu, J., Liu, J.T., Wang, X., 2012. Sediment trapping of turbidity maxima in the Changjiang Estuary. Mar. Geol. 303–306, 14-25.

Xu, K., Chen, Z., Zhao, Y., Wang, Z., Zhang, J., Hayashi, S., Murakami, S., Watanabe, M., 2005. Simulated sediment flux during 1998 big-flood of the Yangtze (Changjiang) River, China. J. Hydrol. 313, 221-233.

Yang, S.L., Belkin, I.M., Belkina, A.I., Zhao, Q.Y., Zhu, J., Ding, P.X., 2003a. Delta response to decline in sediment supply from the Yangtze River: evidence of the recent four decades and expectations for the next half-century. Estuar. Coast. Shelf Sci. 57, 689-699.

Yang, S.L., Friedrichs, C.T., Shi, Z., Ding, P.X., Zhu, J., Zhao, Q.Y., 2003b. Morphological response of tidal marshes, flats and channels of the Outer Yangtze River mouth to a major storm. Estuaries 26, 1416-1425.

Yang, S.L., Zhang, J., Zhu, J., Smith, J.P., Dai, S.B., Gao, A., Li, P., 2005. Impact of dams on Yangtze River sediment supply to the sea and delta intertidal wetland response. Journal of Geophysical Research: Earth Surface 110, F3006.

Yang, S.L., Zhang, J., Dai, S.B., Li, M., Xu, X.J., 2007. Effect of deposition and erosion within the main river channel and large lakes on sediment delivery to the estuary of the Yangtze River. Journal of Geophysical Research: Earth Surface, 112(F2): F02005.

Yang, S.L., Liu, Z., Dai, S.B., Gao, Z.X., Zhang, J., Wang, H.J., Luo, X.X., Wu, C.S., Zhang, Z., 2010. Temporal variations in water resources in the Yangtze River (Changjiang) over the Industrial Period based on reconstruction of missing monthly discharges. Water Resour. Res. 46, W10516.

Yang, S.L., Milliman, J.D., Li, P., Xu, K., 2011. 50,000 dams later: Erosion of the Yangtze River and its delta. Global Planet. Change 75, 14-20.

Yang, S.L., Milliman, J.D., Xu, K.H., Deng, B., Zhang, X.Y., Luo, X.X., 2014. Downstream sedimentary and geomorphic impacts of the Three Gorges Dam on the Yangtze River. Earth-Sci. Rev. 138, 469-486.

YEWAB (Yangtze Estuary Waterway Administration Bureau), Research report on the dredging operation optimization of Changjiang Estuary Deep Navigation Channel Project, Shanghai, 2008, p. 54 (in Chinese).

Ying, X., Ding, P., Wang, Z.B., Van Maren, D.S., 2011. Morphological Impact of the Construction of an Offshore Yangshan Deepwater Harbor in the Port of Shanghai, China. J. Coastal Res., 163-173.

Yun, C.X., 2004. Recent Evolution of the Yangtze Estuary and Its Mechanisms. China Ocean Press, Beijing, China (in Chinese).

Zhang, M., Townend, I., Zhou, Y., Cai, H., 2016. Seasonal variation of river and tide energy in the Yangtze estuary, China. Earth Surf. Proc. Land. 41, 98-116.

Zhou, Z., Coco, G., Townend, I., Olabarrieta, M., van der Wegen, M., Gong, Z., D Alpaos, A., Gao, S., Jaffe, B.E., Gelfenbaum, G., He, Q., Wang, Y., Lanzoni, S., Wang, Z., Winterwerp, H., Zhang, C., 2017. Is "Morphodynamic Equilibrium" an oxymoron? Earth-Sci. Rev. 165, 257-267.

Zhu, L., He, Q., Shen, J., Wang, Y., 2016. The influence of human activities on morphodynamics and alteration of sediment source and sink in the Changjiang Estuary. Geomorphology, 273: 52-62.

Figures

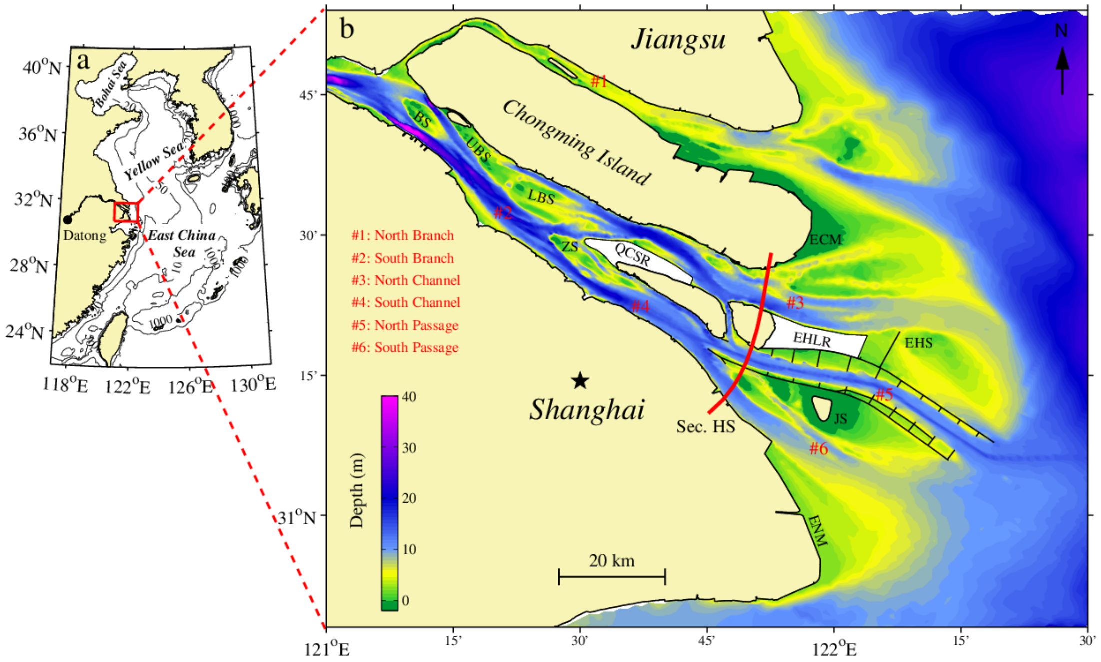

Fig. 1. (a) The location of the Yangtze Estuary on the western coast of the East China Sea (rectangle); (b) The Yangtze Estuary with bathymetry observed in 2010 under mean sea level (MSL). The thick line in (b) represents the HS section for mud flux computation. BS: Baimao Shoal; UBS: Upper Biandan Shoal; LBS: Lower Biandan Shoal; ZS: Zhongyang Shoal; ECM: East Chongming mudflat; EHS: East Hengsha Shoal; JS: Jiuduansha Shoal; ENM: East Nanhui mudflat; QCSR: Qingcaosha Reservoir; and EHLR: East Hengsha Land Reclamation.

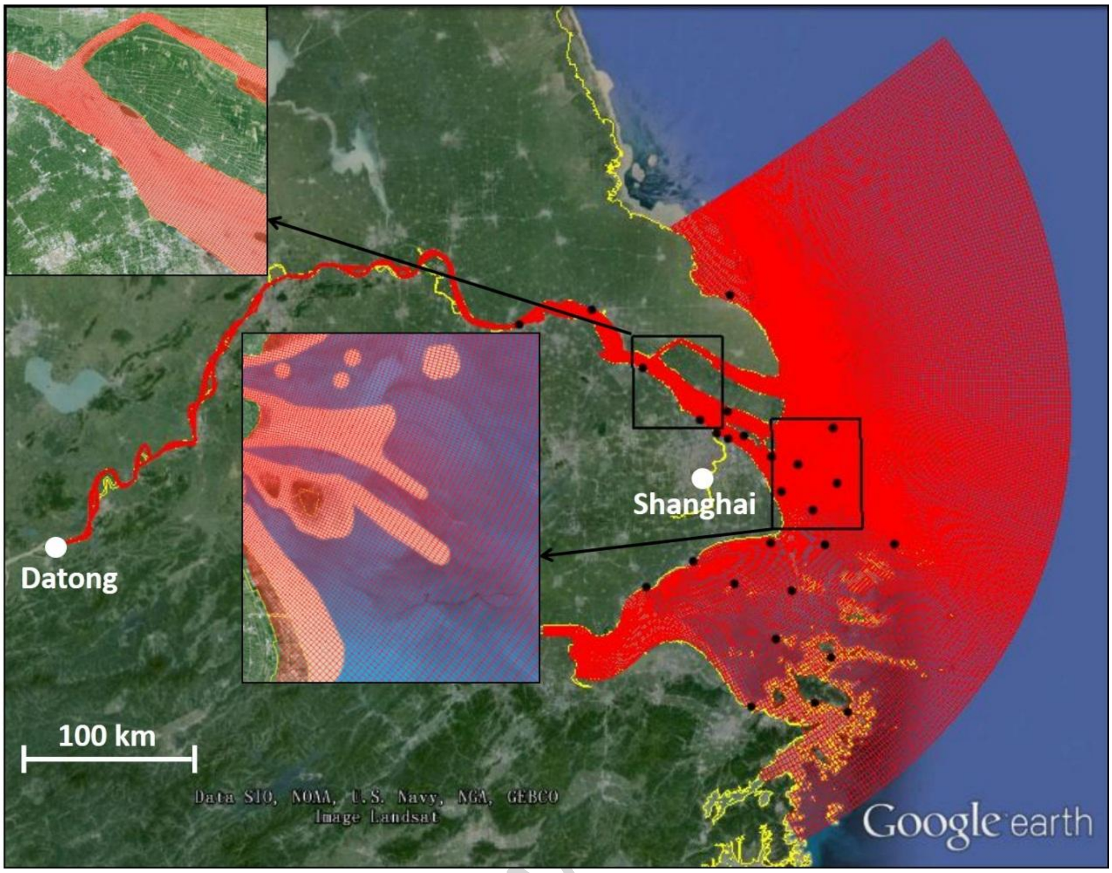

Fig. 2. Model domain and grids with two zoomed-in areas, the South Branch and the mouth bar area. The black circles represent the tidal-gauge stations for validation of the tidal harmonic constants.

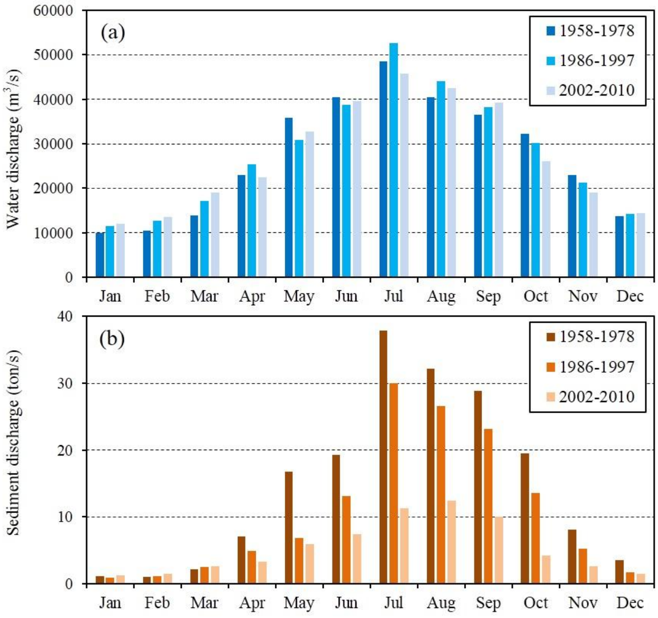

Fig. 3. Monthly averaged water discharge (WD) (a) and suspended sediment discharge (SSD) (b) during three periods (1958-1978, 1986-1997 and 2002-2010).

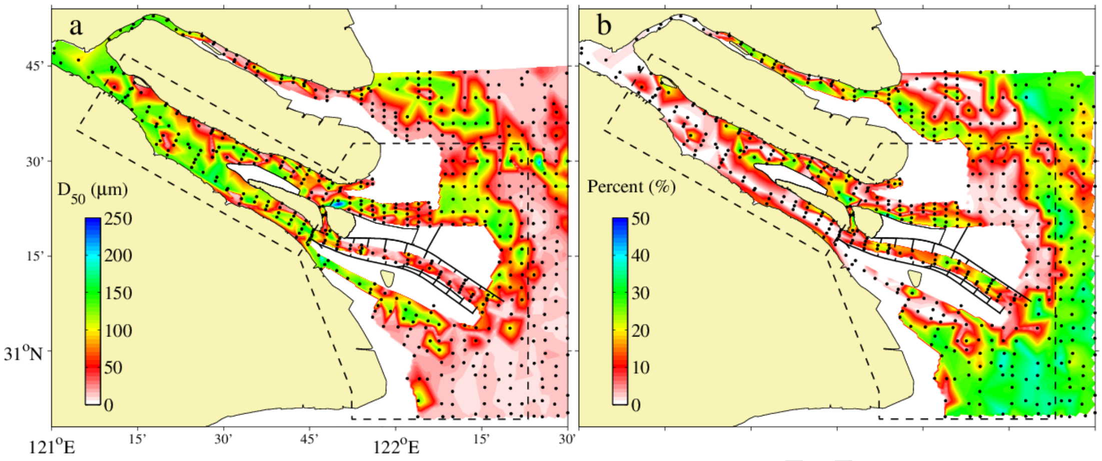

Fig. 4. Locations where the bed surface sediment samples (dots) were obtained and the distribution of median grain size (D_{50}) (a) and clay content (%) (b). The dashed lines denote the defined boundaries of the inner estuary and the mouth bar area.

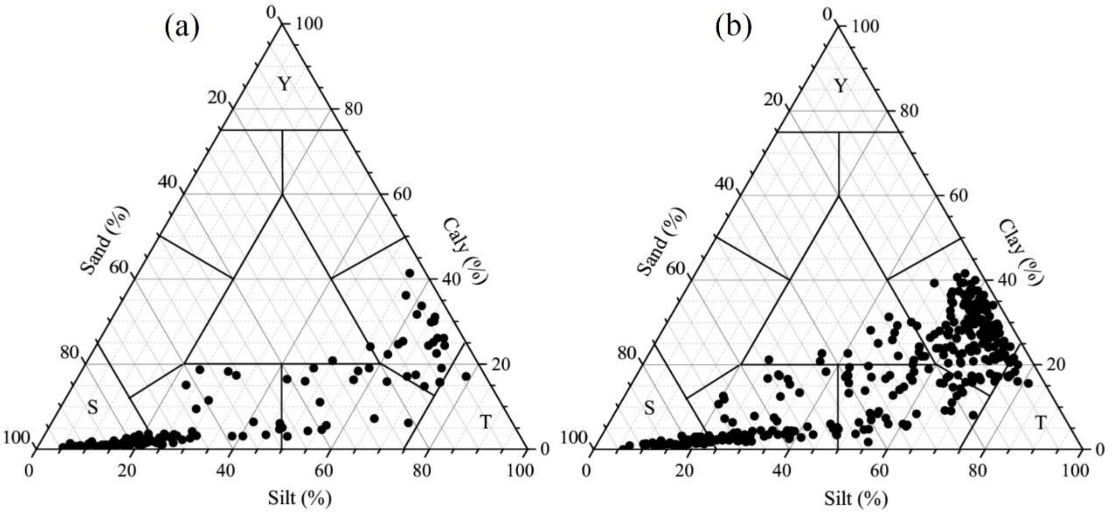

Fig. 5. Ternary diagram of the sand/silt/clay (S/T/Y) proportions of 123 samples from the inner estuary (a) and 330 samples from the mouth bar area (b), as shown in Fig. 4.

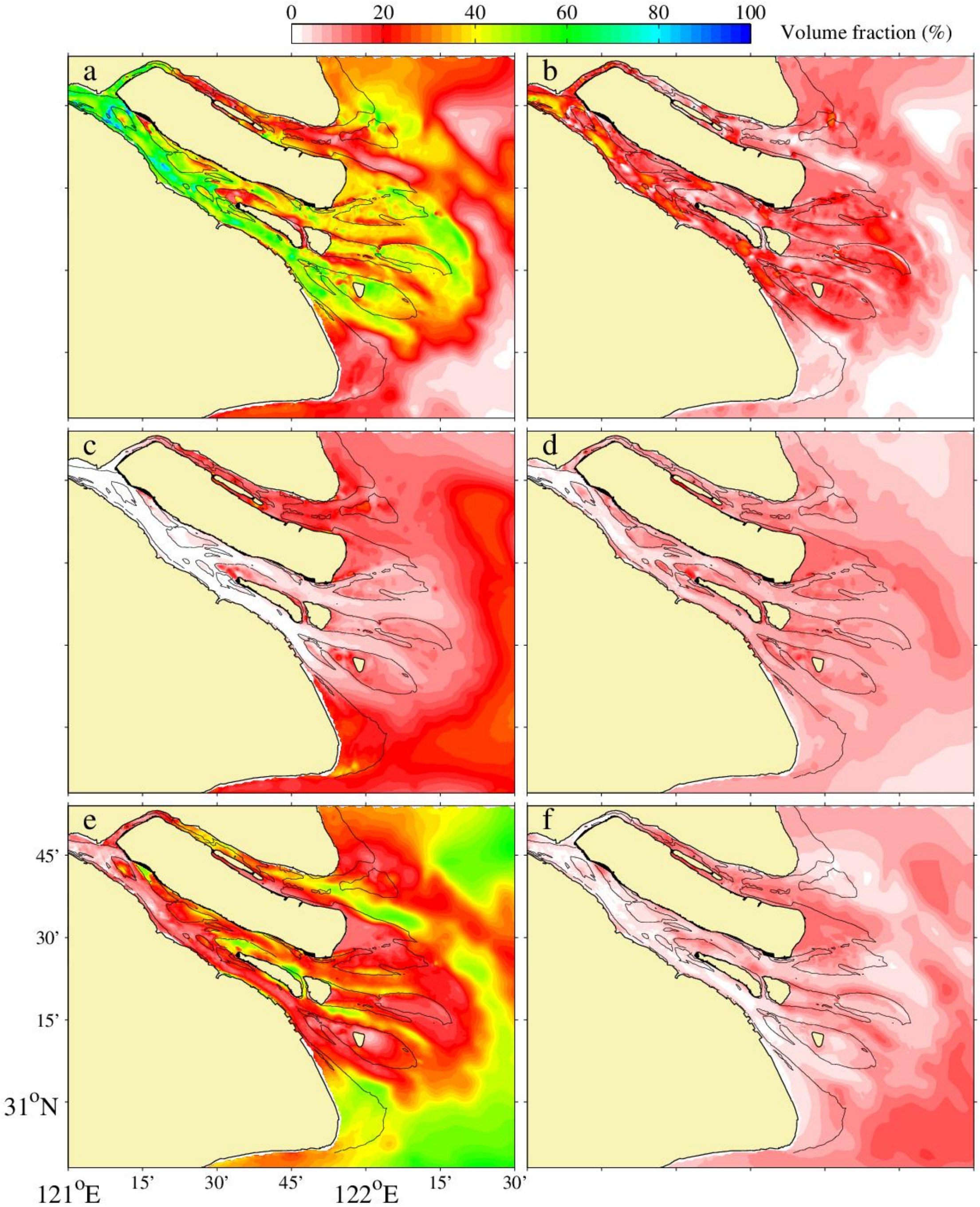

Fig. 6. Spatial distributions of the initial sediment volume fraction in the 2002-2010 hindcast case achieved using the Bed Composition Generation approach (Van der Wegen et al., 2011b): (a) s1 fraction, (b) s2 fraction, (c) m1 fraction, (d) m2 fraction, (e) m3 fraction and (f) m4 fraction. The 5 m isobaths of 2002 are shown by thin black lines.

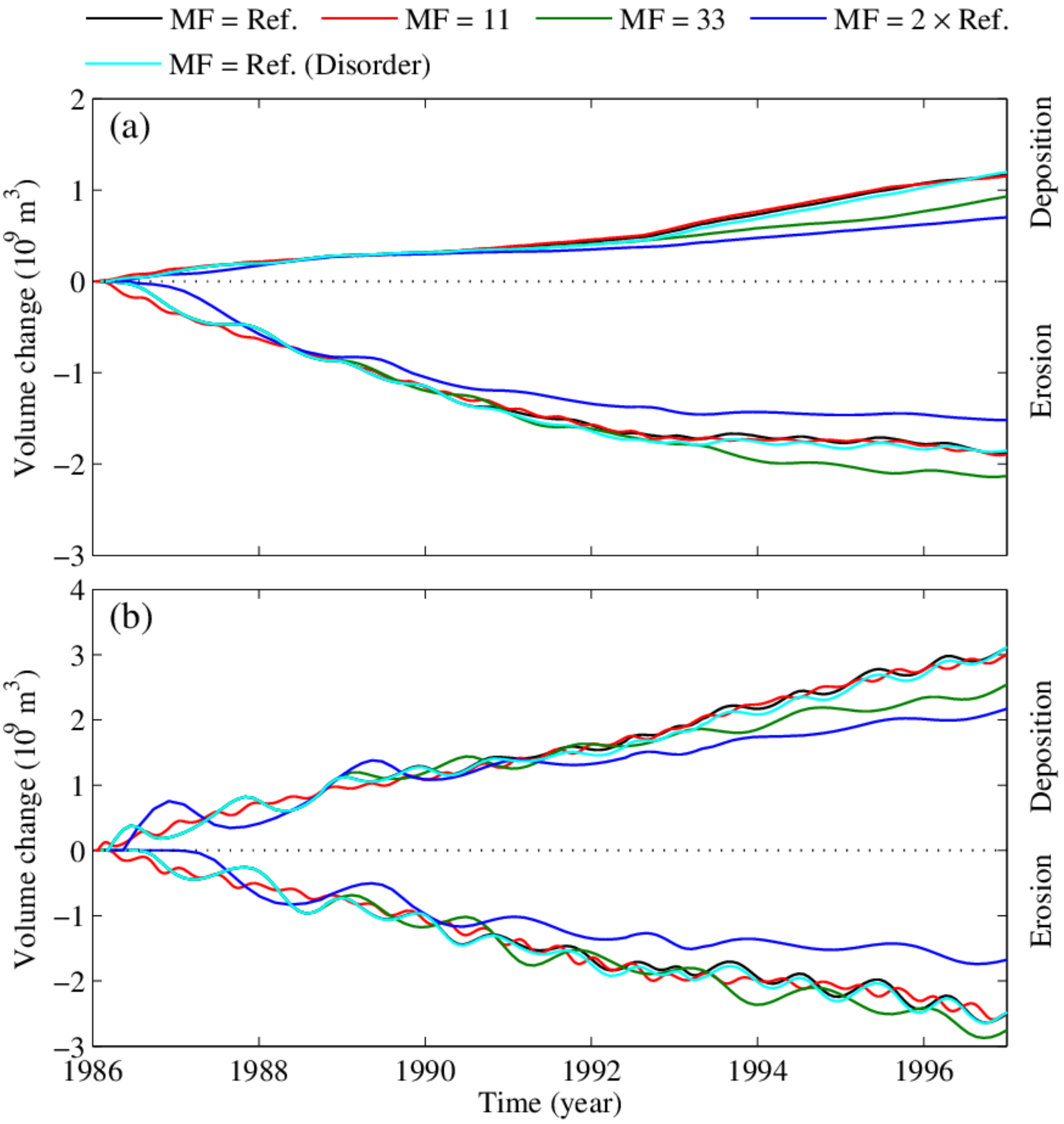

Fig. 7. Sensitivity of the morphological factor (MF) to sediment volume changes in the inner estuary (a) and the mouth bar area (b) for the 1986-1997 hindcast case. The MF values of the reference case are shown in Table 1.

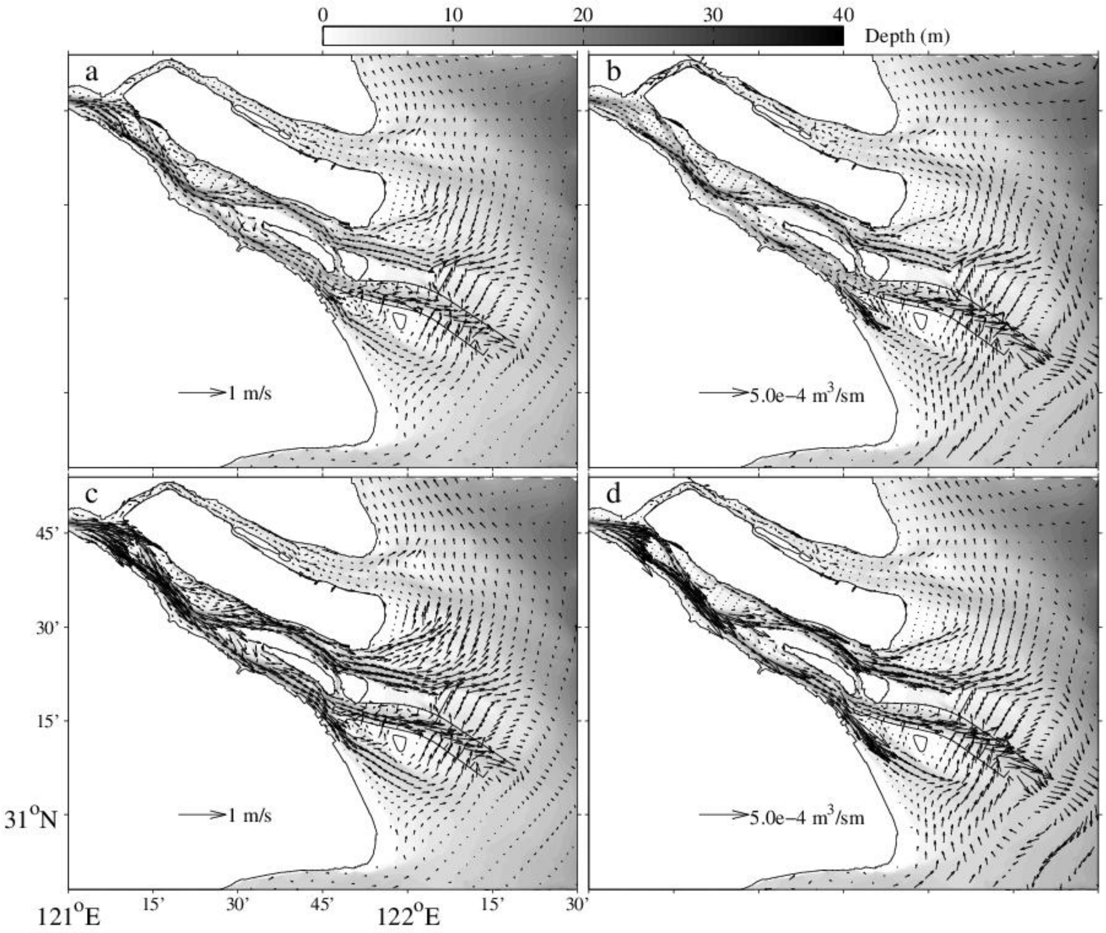

Fig. 8. Residual current (a, c) and total sediment transport (b, d) of the 2002-2010 hindcast case during the dry (a, b) and wet seasons (c, d) with bathymetry observed in 2002 under MSL.

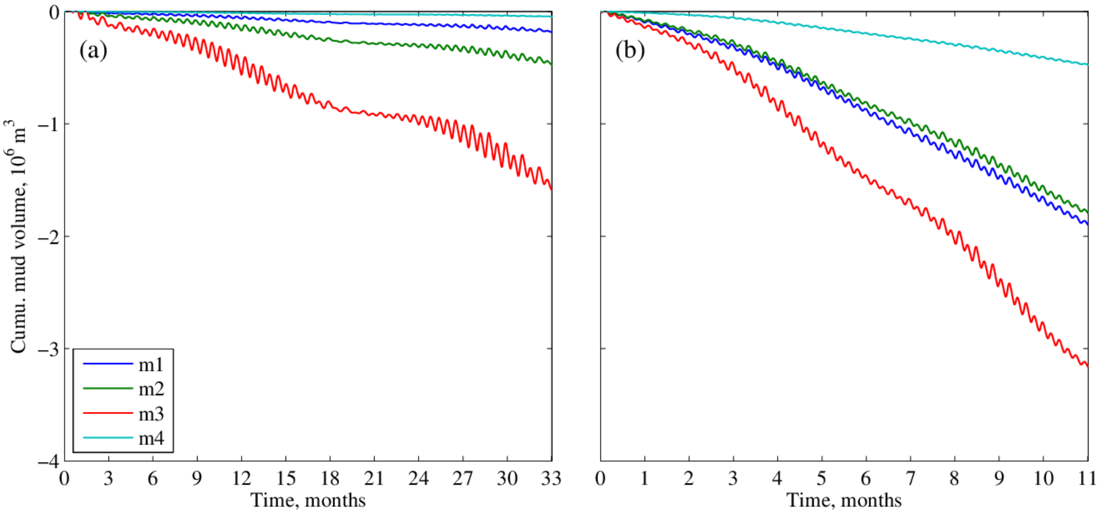

Fig. 9. Cumulative sediment fluxes of the four mud fractions through the HS section during the dry (a) and wet seasons (b) in the 2002-2010 hindcast case (see Fig. 1 for the location of the section). Negative values indicate seaward transport.

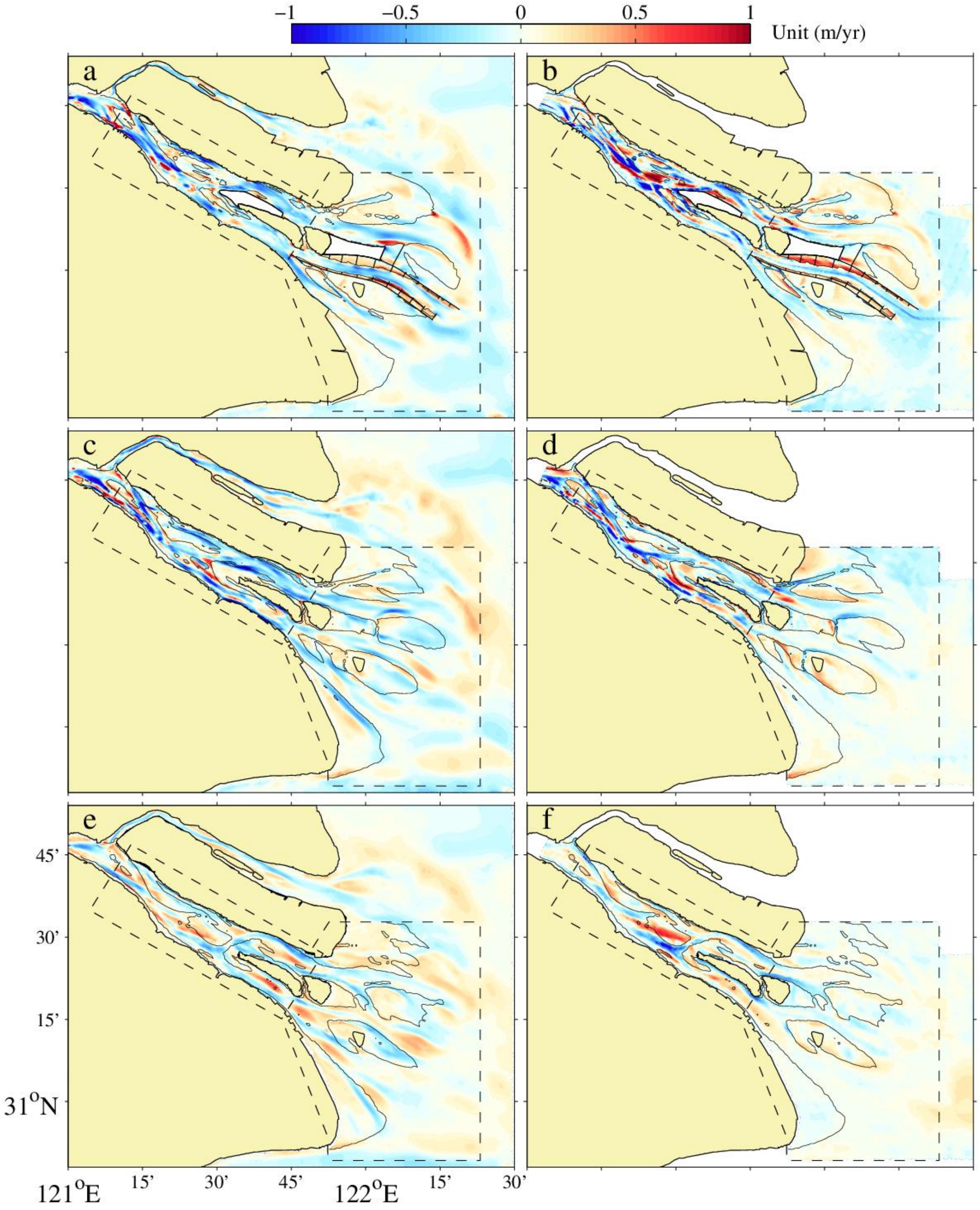

Fig. 10. Modeled (a, c, e) and observed (b, d, f) erosion (negative) and deposition (positive) patterns in the Yangtze Estuary in 2002-2010 (a, b), 1986-1997 (c, d) and 1958-1978 (e, f). The thin solid lines denote the observed 5 m isobaths of the last year, and the dashed lines denote the defined boundaries of the inner estuary and the mouth bar area.

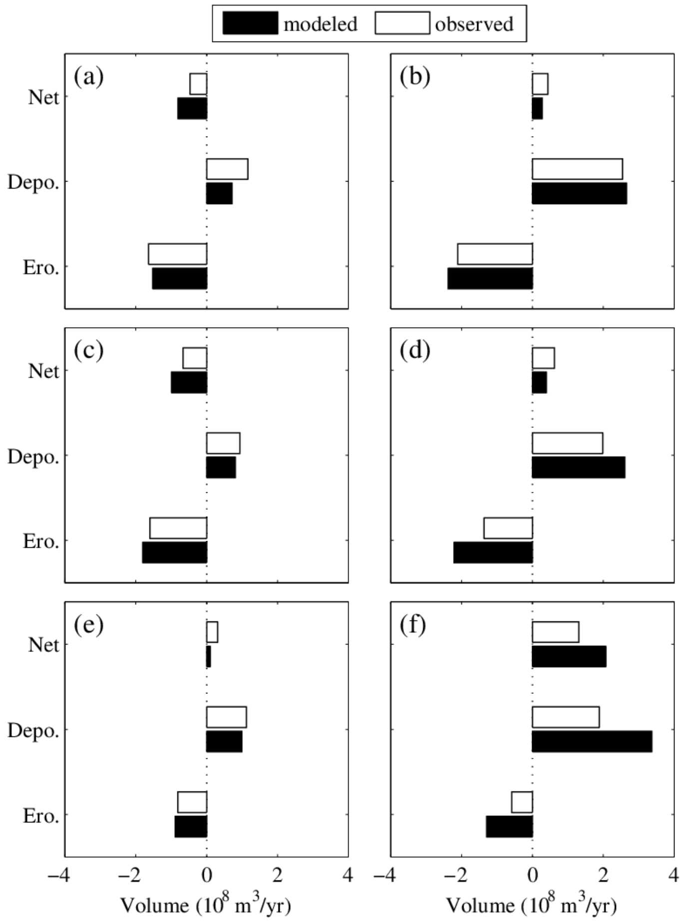

Fig. 11. Model/data comparisons of erosion, deposition and net sediment volume changes in the inner estuary (a, c, e) and the mouth bar area (b, d, f) in 2002-2010 (a, b), 1986-1997 (c, d) and 1958-1978 (e, f).

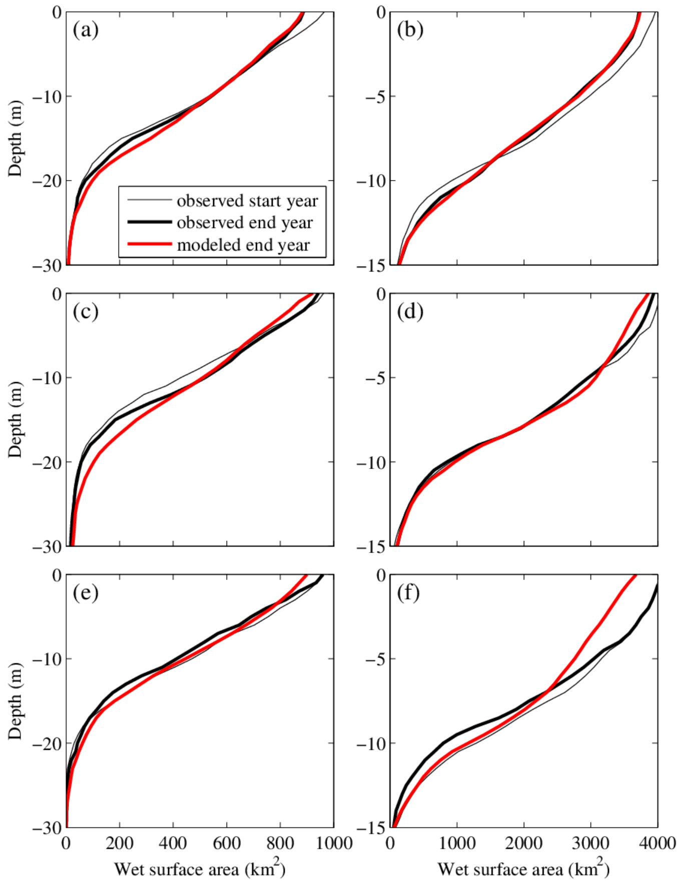

Fig. 12. Model/data comparisons of hypsometry curves for the inner estuary (a, c, e) and mouth bar area (b, d, f) in 2002-2010 (a, b), 1986-1997 (c, d) and 1958-1978 (e, f).

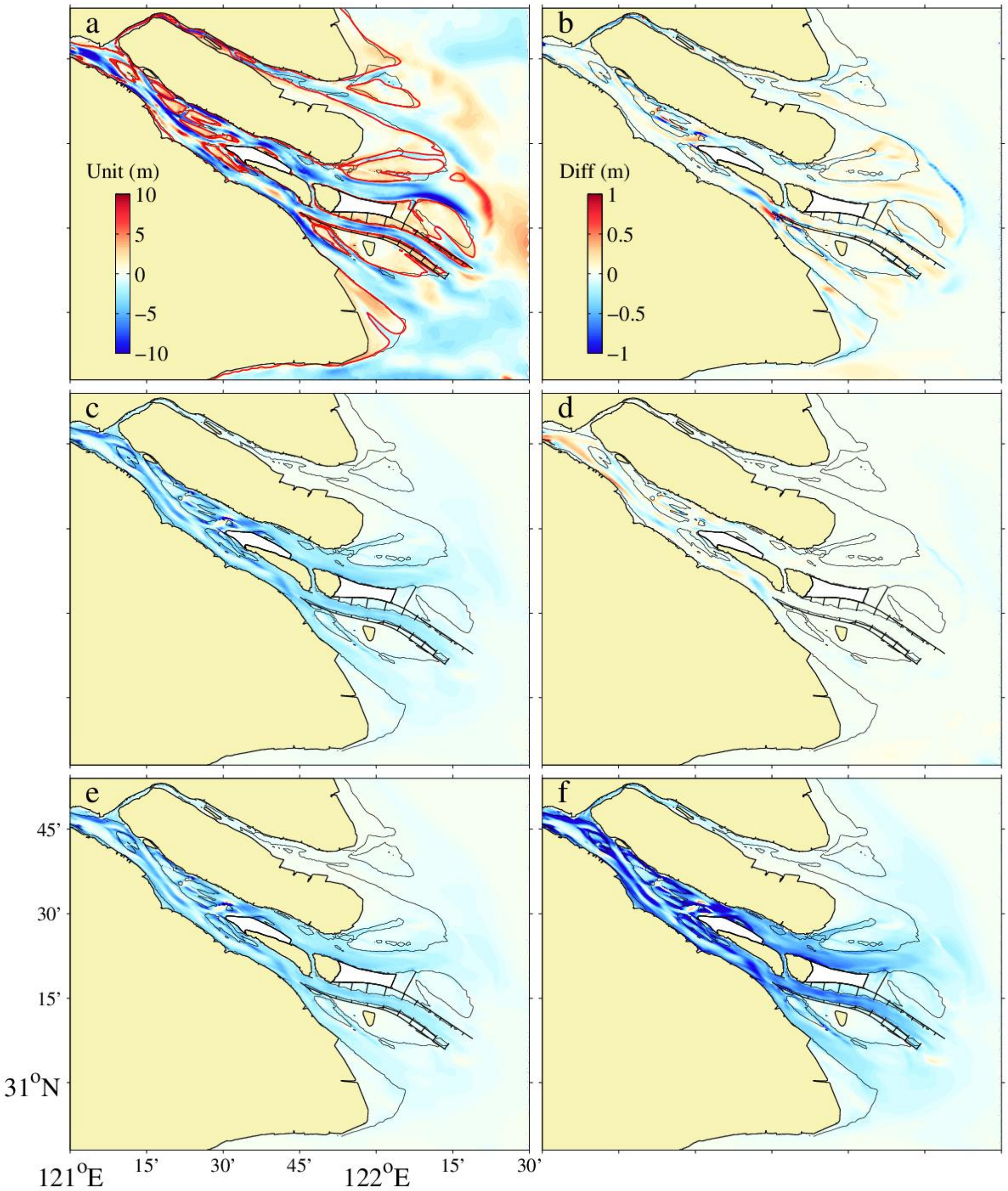

Fig. 13. Erosion and deposition patterns of the forecast (2010-2030) Scenario 4 (a) and the morphological change differences between Scenarios 1 and 0 (b), Scenarios 2 and 0 (c), Scenarios 3 and 1 (d), Scenarios 4 and 3 (e) and Scenarios 5 and 3 (f). (c) - (f) share the range of differences with (b). The thin and thick lines represent the 5 m isobaths of 2010 and 2030, respectively.

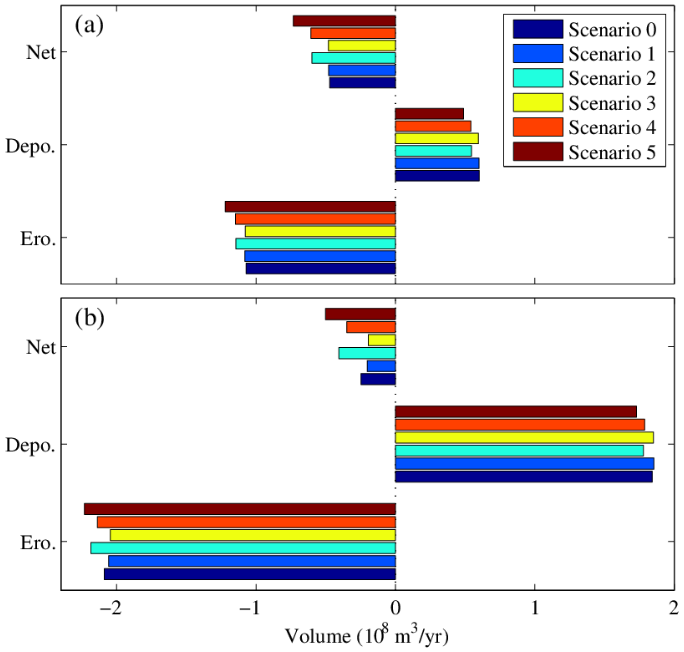

Fig. 14. Forecast scenarios of erosion, deposition and net sediment volume changes in the inner estuary (a) and the mouth bar area (b).

Tables

Table 1. Six periods (P1-P6) in the river input schematization and model parameters including the water discharge (WD), suspended sediment discharge (SSD) and suspended sediment concentration (SSC) at Datong, their corresponding calendar, and simulation times, and the morphological factors (MF) used in the three hindcast cases (1958-1978, 1986-1997 and 2002-2010). The MFs of the six periods for forecast 2010-2030 and the annual values of WD, SSD, SSC and MF are also given.

		P1	P2	P3	P4	P5	P6	Annual
Calendar month		Dec., Jan., Feb.	Mar.	Apr., May, Jun.	Jul.	Aug., Sep.	Oct., Nov.	
Simulation time (month)		1	0.5	1.5	1	1	1	6
1958-1978	WD ($m^3\ s^{-1}$)	11415	13998	33075	48419	38469	27633	27409
	SSD ($ton\ s^{-1}$)	1.890	2.204	14.387	37.911	30.565	13.774	469[a]
	SSC ($kg\ m^{-3}$)	0.166	0.157	0.435	0.783	0.795	0.498	0.543
	MF	60	40	40	20	40	40	40
1986-1997	WD ($m^3\ s^{-1}$)	12828	17242	31671	52558	41080	25780	28161
	SSD ($ton\ s^{-1}$)	1.275	2.503	8.288	29.967	24.882	9.385	343[a]
	SSC ($kg\ m^{-3}$)	0.099	0.145	0.262	0.570	0.606	0.364	0.386
	MF	33	22	22	11	22	22	22
2002-2010	WD ($m^3\ s^{-1}$)	13290	18975	31630	45754	40886	22568	27265
	SSD ($ton\ s^{-1}$)	1.416	2.596	5.554	11.284	11.199	3.403	169[a]
	SSC ($kg\ m^{-3}$)	0.107	0.137	0.176	0.247	0.274	0.151	0.197
	MF	24	16	16	8	16	16	16
2010-2030	MF	60	40	40	20	40	40	40

[a] The annual SSD is in Mt yr^{-1}.

Table 2. Parameters of the sediment fractions considered in the morphological model

		D_{50} (μm)	τ_{ce} (N m^{-2})	w_s (mm s^{-1})	M (kg m^{-2} s^{-1})
Mud	m1	4	Spatial	0.06	5.0×10^{-5}
	m2	7.5	Spatial	0.14	
	m3	30	Spatial	0.22	
	m4	62.5	Spatial	0.26	
Sand	s1	100	-	-	-
	s2	300	-	-	-

Table 3. Model parameters of the 2010-2030 forecast scenarios including the monthly water discharge (WD) of P1, P5 and P6 (refer to Table1), the annual WD, the annual suspended sediment discharge (SSD), the annual suspended sediment concentration (SSC) at Datong and the relative sea-level rise (RSLR) around the estuary.

Scenarios	Monthly WD (m^3 s^{-1})			Annual WD (m^3 s^{-1})	Annual SSD (Mt yr^{-1})	Annual SSC (kg m^{-3})	RSLR (m)
	P1	P5	P6				
Scenario 0	13290	40886	22568	27265	150	0.174	0
Scenario 1	13290	40886	22568	27265	150	0.174	0.112
Scenario 2	13290	40886	22568	27265	125	0.145	0
Scenario 3	13057	38474	21236	26582	150	0.179	0.112
Scenario 4	13057	38474	21236	26582	125	0.149	0.112
Scenario 5	13057	38474	21236	26582	100	0.119	0.112